Modeling of Envelope Power Spectra for Reference-free Ultrasonic Attenuation Estimation of Soft Tissue

A thesis submitted to the Department of Electrical and Electronic Engineering

of

Bangladesh University of Engineering and Technology

in partial fulfillment of the requirement for the degree of

MASTER OF SCIENCE IN ELECTRICAL AND ELECTRONIC ENGINEERING

by

Md. Hadiur Rahman Khan
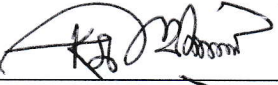
Student ID: 1014062229 P

DEPARTMENT OF ELECTRICAL AND ELECTRONIC ENGINEERING
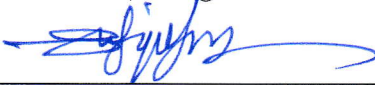
BANGLADESH UNIVERSITY OF ENGINEERING AND TECHNOLOGY

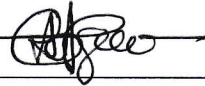August 2018

Approval Certificate

The thesis titled **"Modeling of Envelope Power Spectra for Reference-Free Ultrasonic Attenuation Estimation of Soft Tissue"**, submitted by Md. Hadiur Rahman Khan, Student No.: 1014062229 P, Session: October, 2014, has been accepted as satisfactory in partial fulfillment of the requirement for the degree of Master of Science in Electrical and Electronic Engineering on August 13, 2018.

Board of Examiners

1. _____

   (Dr. Md. Kamrul Hasan)   **Chairman**
   Professor   (Supervisor)
   Department of Electrical and Electronic Engineering
   Bangladesh University of Engineering and Technology
   Dhaka - 1205, Bangladesh

2. _____

   (Dr. Md. Shafiqul Islam)   **Member**
   Professor and Head   (Ex-Officio)
   Department of Electrical and Electronic Engineering
   Bangladesh University of Engineering and Technology
   Dhaka - 1205, Bangladesh

3. _____

   (Dr. Mohammed Imamul Hassan Bhuyian)   **Member**
   Professor
   Department of Electrical and Electronic Engineering
   Bangladesh University of Engineering and Technology
   Dhaka - 1205, Bangladesh

4. _____

   (Dr. A. B. M. Aowlad Hossain)   **Member**
   Professor   (External)
   Department of Electronics and Communication Engineering
   Khulna University of Engineering & Technology
   Khulna - 9203, Bangladesh

Candidate's Declaration

It is hereby declared that this thesis or any part of it has not been submitted elsewhere for the award of any degree or diploma.

Signature of the candidate

_____

Md. Hadiur Rahman Khan

(Student No.: 1014062229 P)

Dedication

To my beloved family, colleagues, and friends.

Acknowledgements

I would like to express my heartfelt gratitude towards Almighty Allah, Most Gracious, Most Merciful, He Who created all things in the best way, and most significantly, the graciousness in my honorable supervisor, Dr. Md. Kamrul Hasan, Professor, Department of Electrical and Electronic Engineering, Bangladesh University of Engineering and Technology (BUET), who provided me with the assiduous support I required. I am greatly indebted to him for his guidance, limitless patience and attention to detail that was decisive for accomplishing this research.

I am also grateful to the Head of the department of Electrical and Electronic Engineering, BUET, for the research lab facilities. I like to thank the students of DSP research lab for their painstaking suggestions and corroborations, especially, Dr. Sharmin Rowshan Ara, Md. Arafat Hussain, and Md. Adib Nahyian.

And I thank my parents for encouraging me all the time, and instilling an intense desire of knowing new things in me. In fact, their continuous inspiration played an important role in my thesis work.

Contents

List of Figures

List of Tables

Glossary

AC	Attenuation coefficient
CIRS	Computerized Imaging Reference Systems, Inc.
DDF	Depth dependent function
FWHM	Full width half maximum
NN	Nearest neighbors
PSF	Point spread function
QUS	Quantitative ultrasound
RF	Radio-frequency
RFAAE	Reference-free average attenuation estimation
ROI	Region of interest
SCAAE	Spectral cross-correlation-based AC estimation
SD	Standard deviation
SNAAE	Spectral normalization-based AC estimation
TGC	Time gain compensation
TMP	Tissue mimicking phantom
TRF	Tissue reflectivity function

Abstract

Estimation of ultrasonic attenuation coefficient (AC) is essential for quantifying and characterizing the features of tissue microstructure. In the conventional AC estimation methods, a well-specified reference phantom is commonly used for minimizing the diffraction and transmit pulse related effects on the ultrasound radio-frequency (RF) echo signal. In this thesis, a novel AC estimation technique is proposed avoiding the need of using any reference data, where the undesired system effects on the RF data are minimized through point spread function (PSF) separation and band-pass filtering of the envelope signal of the tissue reflectivity function (TRF). An improved and computationally efficient non-parametric cepstrum-based technique is used for separating the TRF and PSF from the measured RF signal. The Hilbert transform based temporal envelope is introduced to smooth out the unwanted effects of discontinuity and noise in the TRF and PSF signals. Finally, a band-pass filter based log power approximation technique is applied to estimate the center frequency component of the attenuating TRF envelope power spectra with reduced diffraction effect. Assuming continuity of AC within a small uniform region, an exponentially weighted-average of logarithmic signal power of the neighboring blocks at the center frequency is measured for different depths, with a view to fit a regression line for obtaining an average AC value from its slope. Comparative results of the proposed reference-free AC estimation method with other conventional reference-based methods are presented for tissue-mimicking (TM) phantoms, *in vivo* breast and liver data. For the TM phantoms, the AC estimates using the proposed algorithm are within 10% deviation of the actual values. The obtained results for the normal female breasts, normal human livers, and fatty livers are 0.44 ± 0.23 dB/cm-MHz, 0.55 ± 0.21 dB/cm-MHz, and 0.61 ± 0.20 dB/cm-MHz, respectively, which are consistent with the literature-reported values of AC. Different from reference-based methods, the proposed technique is free from the bias that may result from the dissimilarity between acoustic characteristics of the reference and sample.

Chapter 1

Introduction

In this Chapter, the motivation for the development of a reference data free attenuation estimation method is incorporated. A detailed review of the relevant and widely adopted attenuation estimation techniques reported in the literature is also provided. Later, the primary objectives achieved in this thesis are enlisted. Finally, a short overview of the thesis organization is presented.

1.1   Motivation of the Thesis

The measurement of attenuation coefficient (AC) *in vivo* using the ultrasound pulse-echo system is emerging as a promising technique for quantitative characterization of different pathological states of soft tissue [1]. Unfortunately, its estimation is a challenging task as the received radio-frequency (RF) echo signal is distorted by frequency and depth dependent effects predominantly caused by beam diffraction, tissue backscattering, and convolutional artifacts with the tissue interrogating pulse [2], thereby causing inaccurate diagnosis. However, the local attenuation coefficient (AC) in quantitative ultrasound (QUS) has been studied as an important feature of normal and pathological conditions within biological tissues (e.g. liver, breast).

In the past few decades, for reliable extraction of core QUS parameter AC (β in dB/cm/MHz), numerous time- and frequency-domain techniques [3]–[9] have been intensively considered. Technically, spectral methods (i.e., spectral shift, spectral differ-

ence, hybrid) [5]–[9], of AC estimation from the change of spectral content with depth are favored over time-domain methods (i.e., zero-crossing density, entropy difference, and B-mode image analysis) [3], [4], because of easier correction for equipment-related diffraction effects and frequency-specific estimation. The variance of the estimated AC values by using these methods is related with the parameters such as window length, number of data segments per block, transmit pulse bandwidth, and number of regression points used per attenuation estimation ROI. The major drawback of these methods is the necessity of a reference RF dataset with similar scattering properties and acquisition parameter settings as of the sample RF data for the system effects minimized AC calculation. During the sample dataset collection, when the machine settings (i.e., depth, gain, focus, transmit power, etc.) are continuously varied, a mandatory measurement calibration from the reference dataset is required to reduce system and transducer dependencies. Therefore, these methods might be ineffective to measure unbiased estimates of AC for the sample datasets with no available reference dataset. In addition, simple spectral averaging within large spatial blocks is used in these spectral methods to account for the random scattering effects of sample medium, limiting the applicability of the spectral methods in clinical settings with higher spatial resolution. As the acoustic attenuation is undeniably important in characterization of different pathological states of soft tissue *in vivo*, hence a reference-free high resolution AC measurement method with correction for system effects can lead to a promising technology.

1.2 Attenuation Estimation Techniques: Literature Review

The absorption and scattering phenomena of ultrasound pulse transmitting through the tissue are related to various property values of the medium, which are of great interest for the identification of numerous diseases in soft tissue. In fact the characterization of different case studies of soft tissue *in vivo* [10], [11] using the measurement of acoustic attenuation has been appearing as a prosperous technique in quantitative ultra-

sound (QUS). Moreover, accurate estimates of size, shape and distribution of the tissue backscatterers are also highly dependent on the total attenuation value [12], [13]. The attenuation is estimated by minimizing the difference of entropies in the two segments as the attenuation is continuously compensated (time-gain-compensation (TGC)) at the axial direction for the acquisition of the envelop statistics of the backscattered RF signal [14]. The TGC compensated pulse echoes returning from any point is represented by the brightness of that point on the screen, however, the sharp changes of the envelope signal power under the different levels of attenuating regions represent significant alterations in tissue characteristics. The envelope attenuation profile, obtainable from the RF images, suggests where there is any characterizing variation of tissue profile, for example, in breast [15], liver [16], thyroids [17], and prostate [11]. For example, in the above mentioned tissue regions, AC value of the fatty segments is usually higher than that of the normal segments. Therefore, there is always a need of computationally efficient but effective AC estimation technique in ultrasound research because of its significant importance for non-invasive clinical diagnosis of tissue pathology.

There are several types of echographic signal processing based AC estimation methods that have been studied in literature, can be classified into two fundamental types depending on the way of RF signal analysis (time-domain and frequency-domain analyses). Time-domain AC measurement techniques mainly based on the number of sign changes per unit interval for center frequency estimation of a narrowband signal [3], statistical analysis of ultrasound echo envelope peak (EEP) [18], minimum entropy difference finding of the envelope sample values of pulsed echoes for two adjacent regions [19], and video signal analysis of the clinical B-mode scans [4]. However, all these techniques are vulnerable to depth and frequency dependent system-related artifacts. To be specific, time-domain attenuation estimation methods do not take into account the precise depth-frequency dependent diffraction correction in the backscattered RF signal.

The frequency-domain methods rely on the spectral change with depth, where the correction of frequency specific system-related effects in attenuation estimation can be easily done. In the spectral difference methods, a measure of decay of the loga-

rithmic power spectrum with depth is used to estimate the AC as a function of frequency [20]–[22]. These algorithms are more likely to result in biased estimates due to the variances of the irregular tissue backscatter [2]. For canceling the transfer functions related to the ultrasound system (e.g., diffraction effects, PSF), a reference phantom based normalization process of the sample spectra is implemented in the spectral difference method [7]. The RF datasets of reference phantom and sample need to be collected with the same machine settings (i.e., gain, frequency, depth, focus) for this elimination procedure. In the spectral shift methods, the statistical nature of the spectrum of backscattered RF signal is taken into account, and the spectral shift toward lower frequencies with propagation depth is used to determine the AC [3], [23]–[25]. These methods have difficulty in correcting for local variations (i.e., diffraction effects) during the AC estimation. For more robust and stable AC estimation from the backscattered RF signals having inhomogeneities in tissue structure, a measure of spectral shift of the entire power spectra is provided by the spectral cross-correlation (SCC) [5]. For the correction of diffraction effects of the sample AC estimates in the SCC method, a reference phantom dataset is used in calculating the system effects from the differences between the theoretical and the measured center frequency downshifts of the RF spectrum.

In other spectral methods, such as spectral normalization-based average attenuation estimation (SNAAE) and spectral cross-correlation-based average attenuation estimation (SCAAE) [6], the nearest neighbors are utilized for consistent and coherent AC estimation. Theoretically, the spectral shift algorithms are vulnerable to the diffraction effects, and the spectral difference algorithms are sensitive to backscatter intensity variations. To counteract the drawbacks of these methodologies, a more accurate hybrid algorithm has been used for AC estimation [8]. However, the above-mentioned AC estimation methods have one major disadvantage, necessitating a well-specified reference phantom under the identical transducer and system conditions as in the case of the sample data. In addition, the AC estimation accuracy can be affected by the difference between the effective frequencies of the pulse propagation through the sample and reference medium [26]–[28]. All these facts, as discussed above, lead to the need

for a reference independent AC estimation technique.

In this thesis, a reference-free average AC estimation (RFAAE) technique is proposed, where the main idea is to measure the power-attenuation of the TRF and PSF signals with depth. For separating the TRF and PSF signals from the measured backscattered RF signal, an improved non-parametric cepstrum-based technique is used. In the proposed envelope power spectra modeling, the unwanted depth and frequency dependent diffraction and other system-related effects are counteracted through the band-pass filtering and regression line fitting over the log power spectrum of the estimated envelope signals. It is shown that this modeling can be used to determine a close approximate of the attenuated center frequency component of the power spectrum at a given depth. For further reduction of the system effect (e.g., tissue backscattering) and consistent estimation of the center frequency component, a nearest neighborhood exponential averaging technique is applied. The exponentially weighted logarithmic power estimate of the small uniform tissue portions along the depth is utilized for linear regression line fitting. Finally, the slope of this line is used for calculating the sample average AC. The proposed AC estimator is tested on the backscattered RF data of TM phantom, *in vivo* breast and liver, along with other familiar reference-based AC estimators.

1.3 Objectives of the Thesis

The objectives of this work are:

1. To propose a new technique of reference-free minimization of diffraction effect in the deconvolved backscattered RF signal for ultrasonic attenuation estimation of soft tissue.

2. To develop an improved non-parametric deconvolution method for extracting the tissue reflectivity function (TRF) and the point spread function (PSF) from the measured RF echo signal.

3. To analyze the impact of an exponential weight function in the neighborhood of the interrogating window on the reduction of AC estimation variance.

4. To make a comparative performance study of the proposed method with other reported reference-based techniques using known AC CIRS (Computerized Imaging Reference Systems, Inc., Norfolk, VA) experimental phantom data, and *in vivo* breast and liver data.

1.4   Organization of the Thesis

This thesis consists of four chapters. Chapter 1 is composed of the motivation and objectives of the thesis and the limitations of the existing techniques. In Chapter 2, the basic principle of ultrasound imaging, its system features and concepts are discussed under respective sections. Chapter 3 has the detailed description of the theoretical aspects of the applied reference-free system-related artifacts minimization based average attenuation estimation using a weighted nearest neighbor method. The graphs shown in this Chapter are obtained for uniform CIRS phantom (i.e., type D) with specific attenuation coefficient. In Chapter 4, the experimental results are demonstrated for both the TMP (Tissue-Mimicking-Phantom) and the in-vivo breast and liver data of healthy and fatty categories. Here, the processing of the RF images and the information of the presets of the ultrasound instrument are also represented. Finally, in Chapter 5, concluding remarks and suggestions for future research are provided based on the outcomes and limitations of this thesis work.

Chapter 2

Basics of Medical Ultrasound Imaging

The basic key concepts of medical ultrasound imaging system are briefly described in this Chapter. Specially, the important topics concerning the attenuation estimation are addressed here, including RF echo image formation, array transducers, beam steering and focusing, mathematical system modeling. This chapter is meant to be the foundations for understanding the particular terms related to the estimation of the QUS parameters.

2.1 Basic Principle of Ultrasound Imaging: Background and Literature

Diagnostic medical sonography is the use of non-invasive high frequency ultrasound which has come into applications since late 1950s [29]. Originally, this technology was designed for the investigation in obstetric and gynecologic cases with static, simple black and white, and compound information acquisition techniques termed as A-mode (amplitude mode), B-mode (brightness mode), and M-mode (motion mode) display methods [30]. In addition, broad-band transducer technologies facilitated with multi-channel focus, high resolution scanners, and digital beamforming capabilities such as

Color Doppler and Duplex, were first utilized during the 90s [31]. Because of the continuous research and development, it becomes possible to use the ultrasound imaging as a non-invasive diagnostic tool for the quantitative and functional information gain of the tissue microstructures.

The principle of ultrasound based upon the pulse-echo system where the conversion between electric pulse and sound energy is made with help of ultrasound piezoelectric crystals. Medical ultrasound imaging are basically done with frequency ranges between 2 - 15 MHz [32], much higher than the audible frequency for human being. Ultrasound pulse is usually produced by applying a voltage to a piezoelectric crystal which either expands or contracts frequently. Then, the crystal vibrates accordingly with the variation of the applied voltage. This forward and backward motions result in ultrasound. When ultrasound pulse is reflected from various types of complex microscopic tissue structures in the body and returns to the ultrasound probe, the reverse occurs and the electrical signals generated are analyzed and a grayscale (B-mode) image of region of interest (ROI) is constructed. Here, the final B-mode images are obtained from the raw backscattered RF signals by using a post-processing pipeline including envelope detection, time-gain compensation, and dynamic-range (i.e., logarithmic) compression. Typically, the ultrasound pulse can be distorted, absorbed, detracted and scattered because of the complicated pattern of tissue, which may cause problems getting actual profile of the ROI from the reflected ultrasound.

Ultrasound transducer is moved in lateral dimension while its beam is aimed down the axial direction to generate a B-mode image by scanning the beam in a plane. The information of scanned image can be divided into multiple lines along the lateral direction, and each single line is termed as scan line. The number of scan lines is usually dependent on the number of elements in an array transducer. In addition, the sample number in a scan line along the axial direction is determined by the sampling frequency of the transducer. The entire process is illustrated in three dimensional Fig. 2.1 showing axial (z-axis), lateral (x-axis), and elevation (y-axis) directions. The image resolution in the axial (i.e., z-axis) and lateral (i.e., x-axis) dimensions are proportional to the frequency and beam-width of the ultrasound waveforms, respectively. At a

higher frequency, the axial resolution gets better, but the attenuation of the signal intensity becomes also higher with propagation depth. Therefore, ultrasonic imaging has a trade-off between the image resolution and penetration depth.
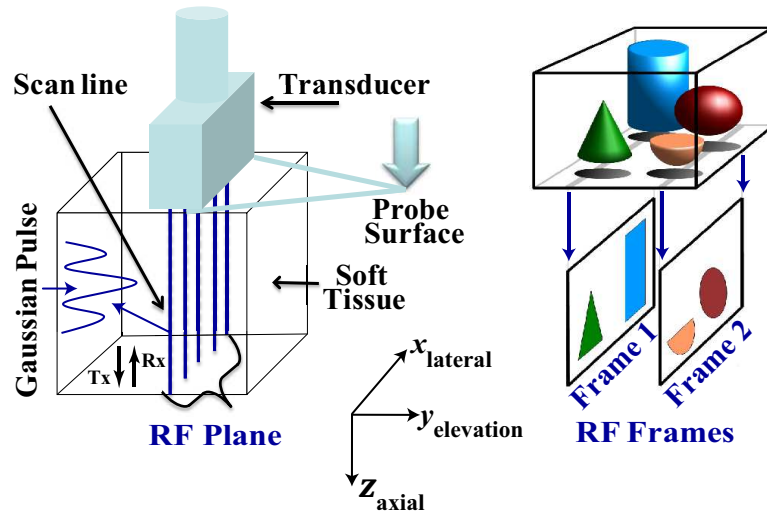
Figure 2.1: Working principle of an ultrasound system.

2.2 Imaging with Array Transducers

A large number of frames are captured from the ROI plane at a time, from which the tissue condition can be observed from different shape and angle. Depending upon the position and shape of the tissue region, a variety of image can be produced with the required probe (e.g., linear array, convex array) as shown in Fig. 2.2. The ROI is picked by firing a set of probe elements (i.e., active elements) located over the interrogated region. The focused beam is swept across the ROI by the electronic activation of contiguous array elements (linear and convex array), without changing the transducer position physically. Focusing and steering of transmitted beam is acquired by delaying the excitation pulses of the individual elements, resulting in a concave beam shape, as shown in Fig. 2.2. The beam focusing can also be achieved during the reception process by delaying and adding the backscattered responses from the multiple elements.

The linear array transducer is used to obtain a rectangular image, where the large

(a) Linear Array Imaging   (b) Convex Array Imaging
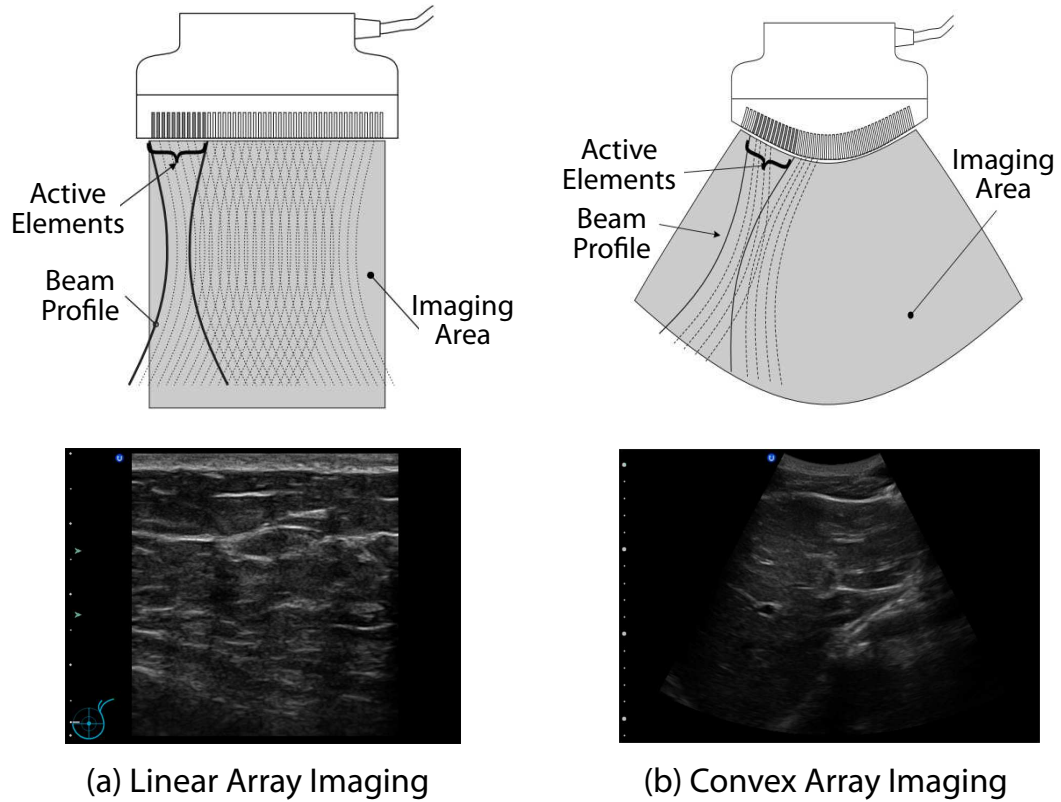
Figure 2.2: Ultrasound probe types and corresponding B-mode images.

arrays employed to get sufficient portion of the ROI. When a comparatively large area needs to be scanned with a smaller array, it can be done effectively by the convex array transducer. For the curved (i.e., convex) array transducers, the initially acquired RF dataset is not geometrically correct to represent the exact tissue structure. Therefore, a scan conversion process is used to map the data from a curvilinear grid to the actual geometry of the tissue. For this process, the geometry and location of the transducer grid and the display grid must be known with respect to each other.

2.3 Mathematical Representation of Imaging System

Based on the first order Born approximation (i.e, assumption of linear propagation and weak scattering) [33], [34], the ultrasound RF images can be modeled as a 2D convolution between the blurring point spread function (PSF) and the tissue reflectivity function (TRF) [35]–[37]. Here, the PSF can be considered as the signal by which tissue information is spread about a point. On the other hand, the TRF is related to the way of how the emitted pulse from the transducer is scattered by the scanned object [1]. Thus, the convolution model can be expressed in the following form [38]:

$$
\begin{aligned}
r(x_l, z_a) &= s(x_l, z_a) * h(x_l, z_a) + u(x_l, z_a), \\
&= \sum_i \sum_j s(x_l - i, z_a - j) h(i, j) + u(x_l, z_a),
\end{aligned}
\tag{2.1}
$$

where $s(x_l, z_a)$, $h(x_l, z_a)$, and $u(x_l, z_a)$ are the PSF, TRF, and additive random noise, respectively; (x_l, z_a) is the lateral and axial position with respect to the probe, and can be Cartesian (for rectangular array transducer) or polar (for convex array transducer) coordinates. The mathematically accurate form of the PSF is determined by the type and properties of the imaging system, whereas the TRF is largely dependent on the type of physical interactions that take place within the medium. By considering the finite beam-thickness, the 2D convolution model could be extended to 3D form model without loss of generality [39].

For the 2D convolution models that exist in the literature [40]–[42], the PSF is considered as shift-variant due to non-uniform focusing, diffraction effects, dispersive attenuation, and phase aberration. In these cases, RF images are usually subdivided into a number of local image segments in the axial dimension by assuming the PSF to be shift-invariant for each segment, whereas the lateral variation of the PSF is considered to be negligible because of aperture weighting (i.e., apodization) and limited amount of lateral data compared to the axial information [36]. Therefore, it is possible to counteract the problem of non-stationary global convolution model by several quasi-

stationary local 1D convolution models. Specifically, attenuation estimation techniques of soft tissue reliably depend on the 1D convolution model by providing an optimal balance between estimation accuracy and computational efficiency [43]. Taking into account all these remarks, the model (2.1) can be approximated as

$$r_i(z_a) = s_i(z_a) * h_i(z_a) + u_i(z_a) = \sum_j s_i(z_a - j)h_i(j) + u_i(z_a), \quad j = 1, 2, \dots \quad (2.2)$$

where $s_i(z_a)$, $h_i(z_a)$, and $u_i(a)$ are the axial smoothing kernel (i.e., PSF), tissue response (i.e., TRF), and Gaussian noise associated with the i-th scan line.

Chapter 3

Average Attenuation Estimation of Soft Tissue

Generally, the usefulness of any AC estimation method can be evaluated by investigating how effectively the minimization process of the diffraction, PSF, and backscattering effects in the RF data are accomplished. The novelty of the proposed Reference-free Average Attenuation Estimation method is that AC can be measured from the soft tissue with proper system effects minimization where no reference data is required. In this chapter, a detailed discussion of the new methodology is provided with appropriate signal processing routines and step-wise reasoning.

3.1   Problem Formulation

Modeling of the back-scattered RF signal and rational use of the envelopes of its constituent signals (i.e., TRF and PSF) are the key to devise a technique for reducing the undesired system effects in the reference-free estimation of AC. The ultrasound echo signal can be considered as a single-input multiple-output (SIMO) model, where the measured RF signals of multiple scan lines are formed by the spatially varying convolution of the same transmitted pulse with the tissue reflectivity functions in the presence of dispersive attenuation along the axial direction [33], [44]. Usually, AC

value is estimated from small segments within a region of interest (ROI) of the entire RF frame, where the variation of attenuation properties can be ignored [1]. Thus, the quasi-stationary backscattered RF data segment $r_i(n, z)$ of the i-th scan line can be modeled as a convolution of the ultrasound pulse or PSF $s(n)$ with the windowed TRF $h_i(n, z)$ at a depth z [44], [45], i.e.,

$$r_i(n, z) = s(n) * h_i(n, z). \tag{3.1}$$

Now, the received RF signal power spectrum $P_{R_i}(f, z)$ of the segmented data $r_i(n, z)$, can be expressed in frequency domain as [2]

$$P_{R_i}(f, z) = P_S(f) \cdot P_{H_i}(f, z) \tag{3.2}$$

with

$$P_{H_i}(f, z) = P_{D_i}(f, z) \cdot P_{B_i}(f, z) \cdot P_{A_i}(f, z). \tag{3.3}$$

Here, $P_S(f)$ is the transmit pulse intensity spectrum, and $P_{H_i}(f, z)$ is the tissue reflectivity intensity spectrum of the i-th scan line segment; $P_{H_i}(f, z)$ consists of beam focusing related diffraction term (i.e., $P_{D_i}(f, z)$), spectral contribution of tissue backscatters (i.e., $P_{B_i}(f, z) = P_{B_i}(f)$) within the homogeneous and isotropic ROI, and frequency dependent attenuation in the soft tissue along the transmitting path (i.e., $P_{A_i}(f, z)$). In (3.2), it is assumed that the data segment of the RF echo signals is much smaller than the focal length of the transducer, and hence the variations of the ultrasound field (i.e., beam diffraction) within this segment may be ignored [2], [8]. In order to estimate AC using (3.2), the depth and frequency dependent system effects (i.e., $P_S(f)$, $P_{D_i}(f, z)$, and $P_{B_i}(f, z)$) need to be reduced from $P_{R_i}(f, z)$.

In the traditional reference-based AC estimation methods [2], [7], the undesired system effects given in (3.2) are generally minimized by spectral normalization as in the following:

$$
\begin{aligned}
10log\left[\frac{P_{R_i,2}(f, z)}{P_{R_i,1}(f, z)}\right] &= 10log\left[\frac{P_S(f) \cdot P_{D_i}(f, z) \cdot P_{A_i,2}(f, z) \cdot P_{B_i,2}(f)}{P_S(f) \cdot P_{D_i}(f, z) \cdot P_{A_i,1}(f, z) \cdot P_{B_i,1}(f)}\right], \\
&= 10log\left[\frac{10^{-2\beta_2 fz/10} \cdot P_{B_i,2}(f)}{10^{-2\beta_1 fz/10} \cdot P_{B_i,1}(f)}\right], \\
&= 10log\left[\frac{P_{B_i,2}(f)}{P_{B_i,1}(f)}\right] + 2\Delta\beta fz, \tag{3.4}
\end{aligned}
$$

where $\Delta\beta = (\beta_1 - \beta_2)$, the sample and reference ACs (in dB/cm-MHz) are represented by β_1 and β_2, respectively. The slope (i.e., $2\Delta\beta f$) of the fitted line over (3.4) with depth z, is evaluated at a particular frequency (i.e., center frequency, f_c) to calculate β_2 with the help of known β_1 of the reference dataset. This kind of AC estimation method is highly sensitive to the selection of a reference phantom, because an inappropriate cancellation of the system transfer functions through spectral normalization given in (3.4) can lead to erroneous estimates.

The challenge in a reference-free method is to mitigate the impact of these system-related effects on the accurate estimation of AC, by using only the sample RF data, $r_i(n, z)$.

3.2 Reference-free Average Attenuation Estimation (RFAAE)

The block diagram of the proposed RFAAE technique is illustrated in Fig. 3.1.

The first step towards the reference-free attenuation estimation is the restoration of PSF and TRF signals from the RF signal. This is because in presence of beam diffraction and other random system effects, it is difficult to directly utilize the distorted Gaussian shaped RF spectrum for AC estimation from the derivative of spectral centroid downshift with depth [5]. The random nature of the RF signal spectrum is illustrated in Fig. 3.2 for arbitrary blocks with dimensions of 30λ (axial) $\times$ 2λ (lateral) at 0.50 and 1.00 cm depth of an experimental phantom D (details are available in Table 4.1 of chapter 4), where the spectral averaging of the overlapped gated windows is used along the two directions for reducing the noise artifacts [8]. In contrary, the exponentially decaying nature of the estimated TRF envelope spectrum, as shown in Fig. 3.2 for the two depths, can be exploited effectively to get rid of the influence of system artifacts on AC estimation, through the band-pass filtering of the approximately undistorted power spectrum portion, as explained later in this chapter. Therefore, the center frequency specific attenuation factor can be easily determined after the TRF-PSF separation at different depths.

To separate the TRF and PSF multiplicative spectra, a non-linear and non-parametric computationally efficient transformation (i.e., cepstrum) is utilized. In order to get the cepstral coefficients $c_i(k, z)$, the real part ($Re\{\cdot\}$) of inverse Fourier transform ($\mathcal{F}^{-1}$) of the log-magnitude spectrum is calculated from (3.1) at a depth z. The relation is given by

$$
\begin{aligned}
c_i(k, z) &= Re\{\mathcal{F}^{-1}(\log|R_i(f, z)|)\}, \\
&= Re\{\mathcal{F}^{-1}(\log|S(f)| + \log|H_i(f, z)|)\},
\end{aligned}
\tag{3.5}
$$

As shown in Fig. 3.3(b), the energy of the cepstrum of PSF signal is mostly concentrated at the first few samples (e.g., within 6 samples), whereas the cepstrum of TRF signal is evenly distributed over the entire quefrency range [46]. Therefore, the inverse cepstrum transform of the low-pass liftered quefrency components can be used for recovering a reasonable approximation of the PSF amplitude spectrum. The cut-off
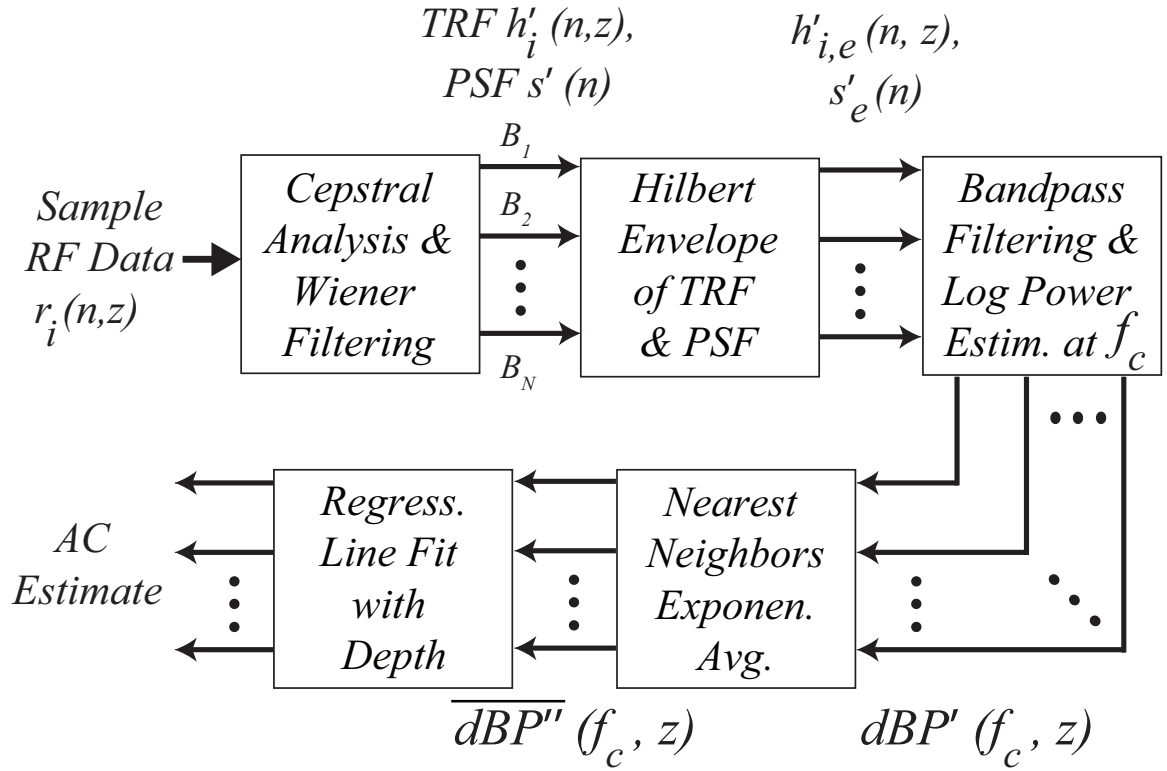
Figure 3.1: Block diagram of the proposed RFAAE algorithm.

quefrency N_c of the low-pass lifter, as displayed in Fig. 3.3(a), is calculated from the inverse of the time (i.e., $\Delta f / f_s$, where $f_s =$ sampling frequency) that is required to rise from 10% to 90% value in the RF log-spectrum. In general, there is no drastic change in the shape of the spectrum due to tissue-related attenuation. For this reason, once the lifter cut-off is determined for the transducer having a specific sampling frequency, then it can be utilized in other situations. Therefore, the liftered cepstrum ($c_p(k)$) is defined as

$$
c_p(k) = \begin{cases} 0.5c_i(k), & k = 0 \\ m_k c_i(k), & 1 \leq k \leq N_c \\ 0, & N_c + 1 \leq k \leq N - 1 \end{cases} \tag{3.6}
$$

where m_k is the multiplier factor of the low-pass lifter, which is dependent on the
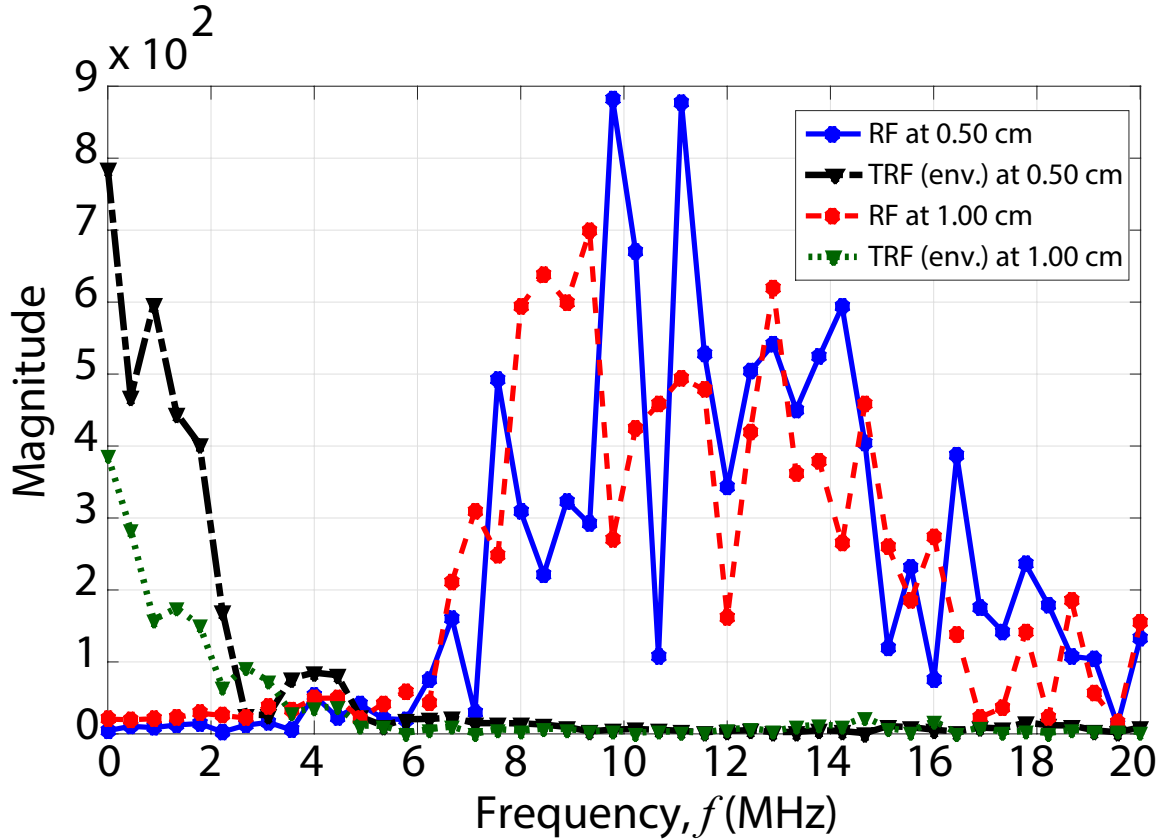
Figure 3.2: Spectra of the RF and the corresponding restored TRF signals at two different depths.

segment length relative to the entire scan line.

Proper selection of a multiplier factor is required for obtaining good approximations of the desired PSF and TRF as evident by the two lifter cases shown in Figs. 3.3(c) and 3.3(d). As shown in Fig. 3.3(c), the estimated PSF (red broken line) using the conventional lifter 1 (i.e., $c_p(0) = c_i(0), m_k = 2$) [47], is an exponentially decaying oscillation rather than the desired Gaussian shaped oscillation as known from [48], and in Fig. 3.3(d), the system effects related TRF (red broken line) obtained from RF
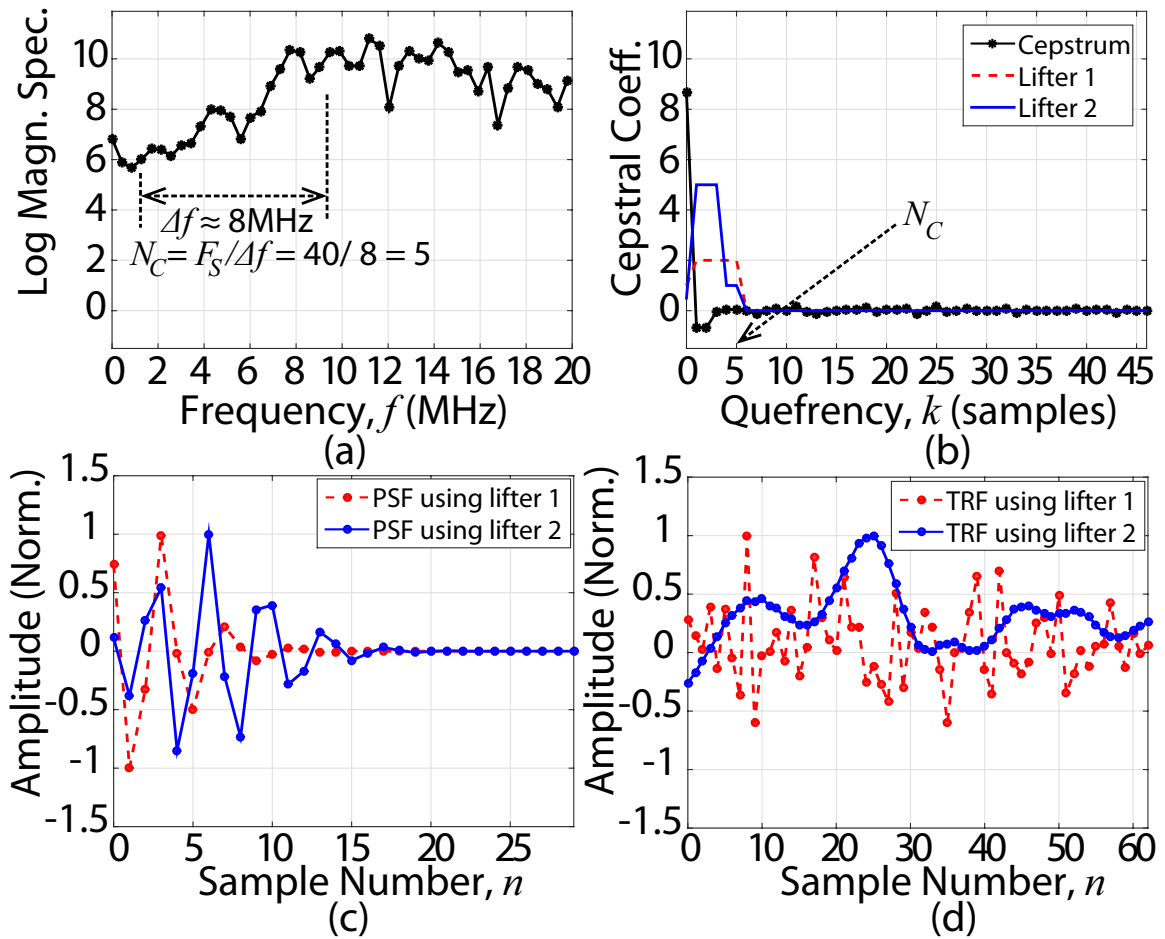
Figure 3.3: Low-pass liftering process for the PSF and TRF separation. (a) The RF Log Magnitude Spectrum, (b) the RF cepstrum, (c) the estimated PSFs, and (d) the estimated TRFs of the corresponding backscattered RF signal ($r_i(n, z)$) with different types of lifter weights using (3.5) and (3.6).

by using the estimated PSF, is also not accurate as evident by the presence of high frequency components under the frequency-dependent attenuation. However, after the use of new lifter 2 (i.e., $c_p(0) = 0.5c_i(0), m_k = 5$ except that $m_{N_c-1} = m_{N_c} = 1$), both the PSF and TRF estimates become closer approximate of the desired shapes. Here, m_k is fixed to 5 depending on the ratio of the number of blocks taken for the entire RF image and for the ROI along the depth. But, m_{N_c-1} and m_{N_c} are set to 1 for minimizing the artifacts in the estimated PSF spectrum related to the sharp cut-off of the liftered cepstrum. The amplitude of the transmitted PSF having finite bandwidth can be fixed when $c_p(0)$ is set to zero, but then the PSF amplitude will be strongly influenced by the out-of-band portion associated with the TRF signal [46]. A reasonable choice preferred in this method is to suppress $c_p(0)$ about 50% of $c_i(0)$ for the PSF measurement using the lifter 2.

Using (3.6), the estimated PSF $s'(n)$ can be obtained as

$$s'(n) = Re\{\mathcal{F}^{-1}(exp(C_p(f)))\}, \tag{3.7}$$

where $C_p(f)$ denote the Fourier spectrum of the liftered cepstrum $c_p(k)$. The PSF spectrum $S'(f)$ calculated from $s'(n)$ by using (3.7) is found to be in accordance with the Gaussian PSF spectrum model discussed in [5], [48].

With the help of the restored PSF $s'(n)$, now a Wiener filter [47] is employed to estimate the TRF $h'_i(n, z)$ in the following way:

$$H'_i(f, z) = R_i(f, z) \cdot G(f), \tag{3.8}$$

$$G(f) = \frac{S'^*(f)}{|S'(f)|^2 + NSR}, \tag{3.9}$$

where the Fourier spectra of the backscattered RF and the estimated TRF and PSF signals are denoted by $R_i(f, z)$, $H'_i(f, z)$, and $S'(f)$, respectively, and $G(f)$ is a simple Wiener filter. The parameter NSR is the noise-to-signal power ratio, which can be set to a specified value depending on the measured RF data. Finally, by performing inverse Fourier transform of (3.8), the TRF $h'_i(n, z)$ can be recovered.

After the TRF-PSF estimation of sample RF data segments, the reference-free AC measurement through mitigating the influence of remaining system effects (i.e.,

diffraction, scattering) can be achieved from the band-pass filtered envelope power spectra of the restored signals. At first, a robust envelope based method is introduced in the TRF-PSF modeling to counteract the amplitude and phase disturbances due to system artifacts [49]. The TRF and PSF envelopes, $h'_{i,e}(n, z)$ and $s'_e(n)$, respectively, having the same energy as the actual signal, can be obtained by Hilbert transform [50] as

$$h'_{i,e}(n, z) = |h'_i(n, z) + j\hat{h}'_i(n, z)|, \qquad (3.10)$$

$$s'_e(n) = |s'(n) + j\hat{s}'(n)|, \qquad (3.11)$$

where j is the complex number operator, $|\cdot|$ denotes the modulus, and $\hat{h}'_i(n, z)$ and $\hat{s}'(n)$ are the discrete Hilbert transform of $h'_i(n, z)$ and $s'(n)$ signals, respectively.

For real-time RF data consisting of all the mentioned system effects, the impact of taking temporal envelopes is shown in Figs. 3.4(a)-3.4(c). The spectral components of the signals are shifted towards the baseband by taking envelope as shown by the broken line of the PSF envelope spectrum compared to solid line of the PSF spectrum in Fig. 3.4(f). In a similar way, the TRF envelope spectrum (broken line) is shown in Fig. 3.4(e), where the discontinuity (for example, the spike near 4 MHz) is smoothed out to a certain extent compared to the TRF spectrum (solid line). As evident from the spectra shown in Figs. 3.4(d)-3.4(f), discontinuity smoothing, scaling invariance preservation and elimination of wideband distortion (common case in channel distorted RF data) are obtained through taking the signal's Hilbert envelope [51].

Before applying the band-pass filter on the envelope TRF power spectrum for the center frequency component based AC estimation, the frequency-depth dependent interferences associated with the beam formation and transducer geometry are investigated. For instance, the beam diffraction related correction equation provided in [52], [9] is

$$\widetilde{D}(f, z) = 1 - e^{-j(2\pi/s)}[J_0(2\pi/s) + jJ_1(2\pi/s)]. \qquad (3.12)$$

In (3.12), J_0 and J_1 are the zeroth- and first-order Bessel functions of the first kind, j is the complex number operator, and the Fresnel parameter $s = zv/fa^2$, where z is the
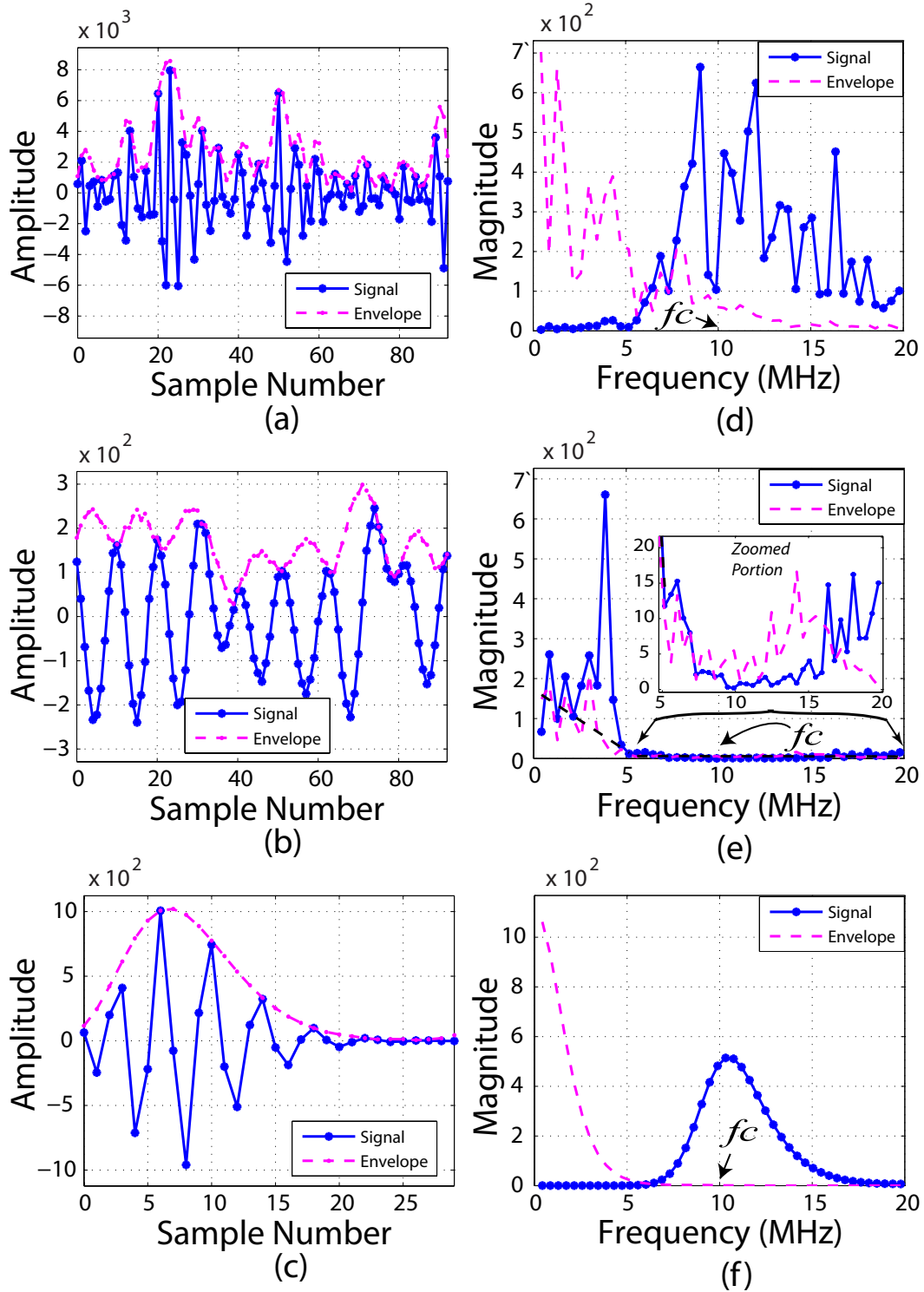
Figure 3.4: The sequences ((a)-(c)) and the corresponding spectra ((d)-(f)) of the RF signal ($r(n)$), the estimated TRF ($h'(n)$) and PSF ($s'(n)$) signals, respectively. In the spectrum, the zero frequency component is not shown (not needed by the envelope power spectra modeling).

distance, v is the speed of ultrasound, f is the frequency, and a is the transducer radius. Eq. (3.12) is illustrated in Fig. 3.5 for an unfocused, single-element transducer with a radius of 4 mm, indicating the transducer beam diffraction $\widetilde{D}(f, z)$ related distortion effects as a function of frequency and depth. It is evident from Fig. 3.5 that the diffraction function $\widetilde{D}(f, z)$ has high-pass characteristics and the lower frequency part of the spectrum (in this case, below 2 MHz) is severely attenuated. At a higher depth, the diffraction related distortion becomes more spread out beyond 2 MHz, but remains much below the center frequency of the band over the depth considered, and hence a proper band-pass filter can be used to recover the undistorted TRF spectrum portion for AC estimation. This is because, unlike the band-limited effects of diffraction, the attenuation factor exists in the entire TRF spectrum.

In order to explore the beam spreading or diffraction pattern for multiple elements, the acoustic pressure field of a linear array transducer having 192 rectangular elements with a center frequency of 10 MHz was calculated using the ultrasound simulation program Field II [53], [54], as shown in Fig. 3.6. The lateral width and spacing (i.e., kerf) of the elements were 2λ and 0.1λ, respectively. The 64 active elements were translated over the aperture for scanning. The beam focus was set at 5.1 cm and the sampling frequency was 40 MHz.

From Figs. 3.6(a) and 3.6(b), it is visible that the magnitude of the pressure field is decreased at the shallow (i.e., segment 1) and deep (i.e., segment 3) regions compared to that at the central focal depth (i.e., segment 2). As a result, in the presence of beam focusing, AC will be underestimated and overestimated in these two regions (i.e., segment 1 and 3), respectively [55], [56]. For the two depths before and beyond the focal zone of the center scan line (i.e., segment 1 and 3), it is observed from Fig. 3.6(c) that the small spectral region between 0 to 2 MHz frequency is largely affected by the beam diffraction, and the rest of the spectra remains approximately unchanged, which is similar to the single-element transducer case.

Now, for the AC estimation model, the TRF envelope power spectrum $P_{H'_{i,e}}(f, z)$ calculated from $h'_{i,e}(n, z)$ by using (3.10) can be expressed as

$$P_{H'_{i,e}}(f, z) \simeq F_e\big(P_{B'_i}(f), P_{D'_i}(f, z)\big) \cdot P_{A'_{i,e}}(f, z), \tag{3.13}$$
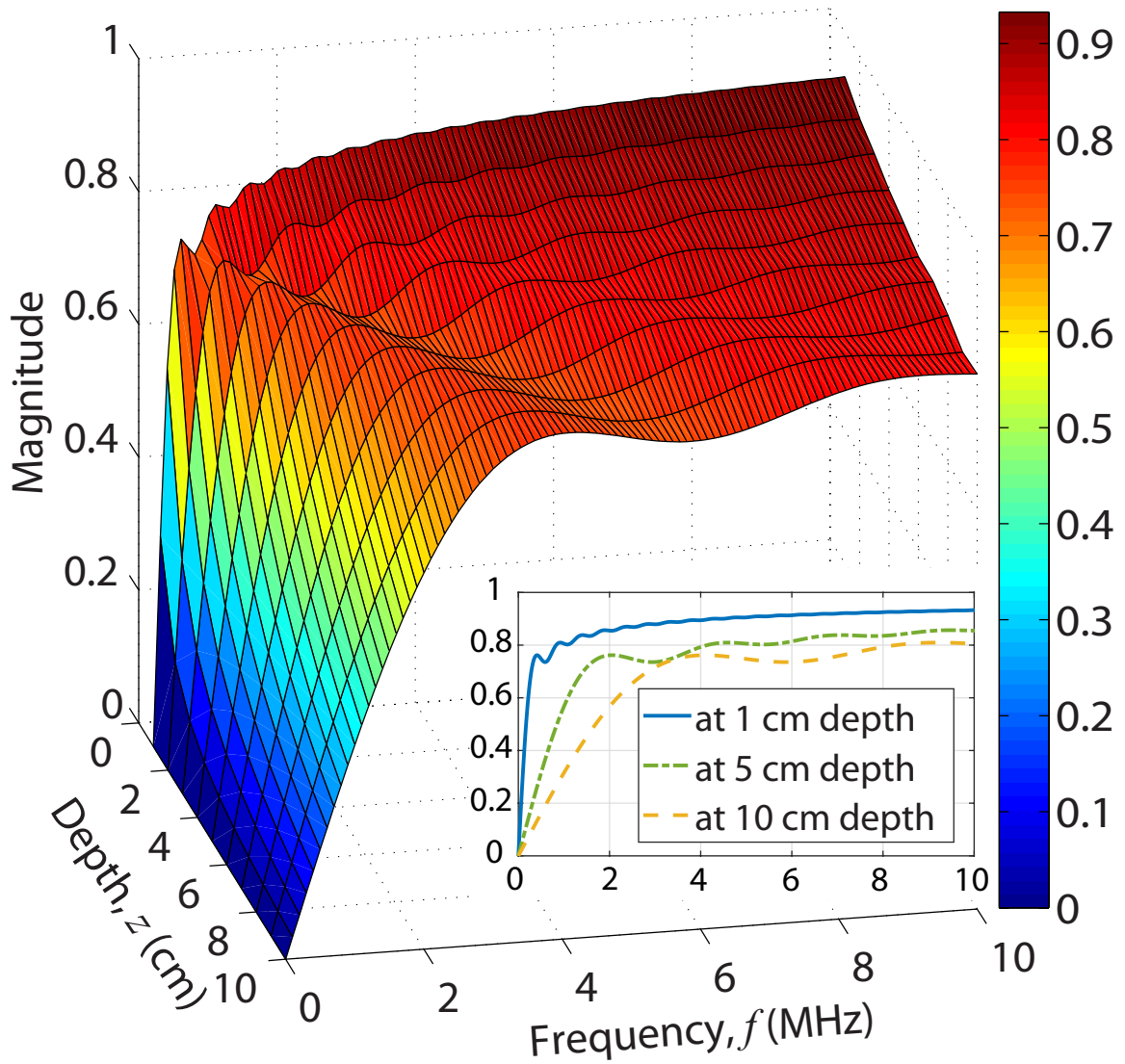
Figure 3.5: Absolute magnitude of the diffraction function $(\widetilde{D}(f, z))$ for a transducer radius of 4 mm.

where the TRF power spectrum $P_{H_i'}(f,z)$ related to its envelope spectrum $P_{H_{i,e}'}(f,z)$
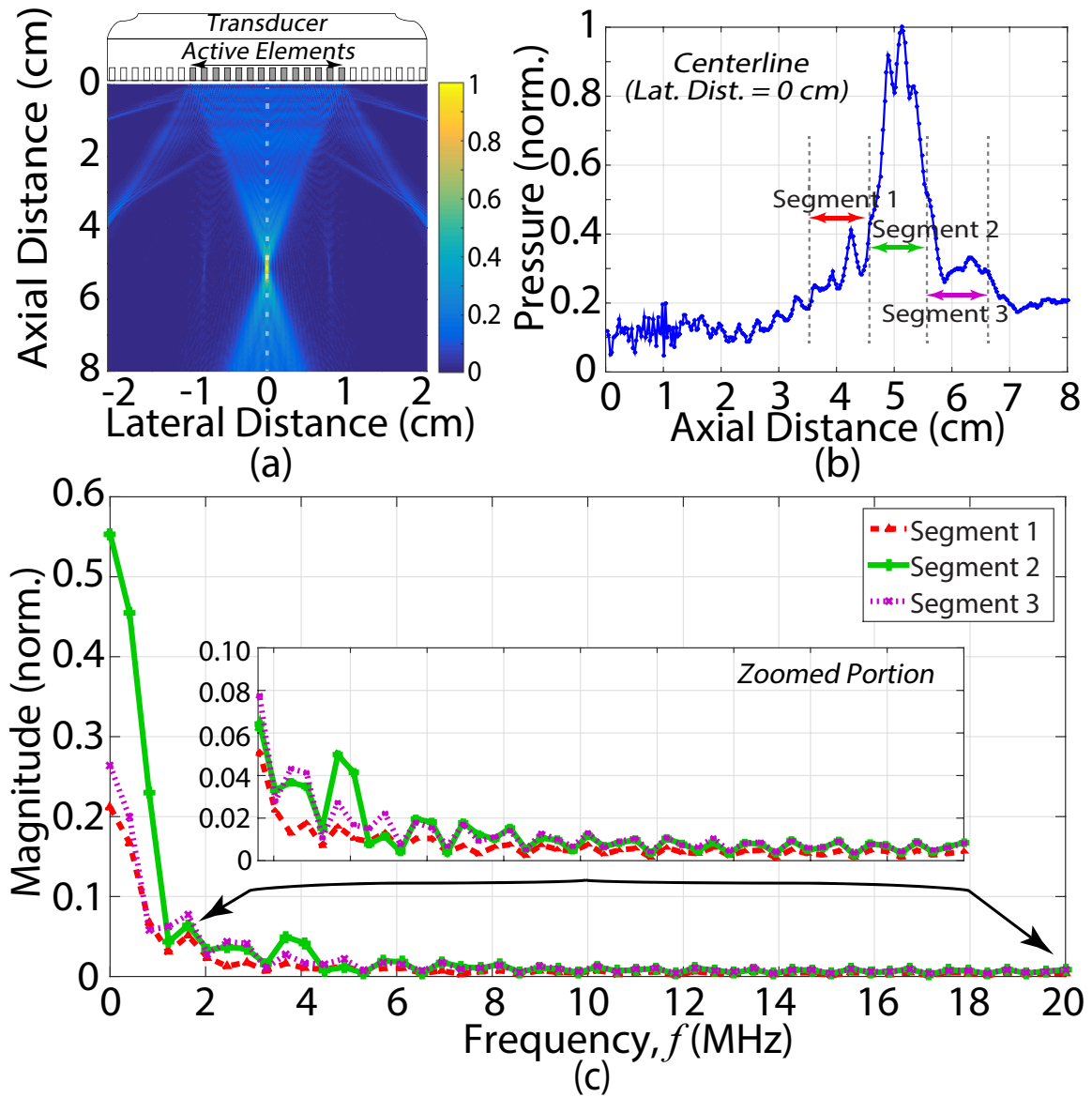
Figure 3.6: The effects of beam diffraction for a multi-element array transducer. (a) The pressure field of a focused linear array transducer with concave beam profile, (b) the normalized pressure of the center-line marked by the vertical white dotted line in the pressure field image, and (c) the estimated spectra of the three segments as shown in (b).

can be written by modifying (3.3) as

$$P_{H'_i}(f, z) \;=\; P_{B'_i}(f) \cdot P_{D'_i}(f, z) \cdot P_{A'_i}(f, z), \tag{3.14}$$

Here, $P_{B'_i}(f)$, $P_{D'_i}(f, z)$, and $P_{A'_i}(f, z)$ are the power spectra of the backscattering, diffraction, and attenuation, respectively, with the effects of estimation incorporated. The function F_e given in (3.13) is for mapping the effects of $P_{B'_i}(f)$ and $P_{D'_i}(f, z)$ in the envelope domain. The attenuation power spectrum $P_{A'_{i,e}}(f, z)$ of the TRF envelope is shown separately in (3.13), because it is closely related to the actual attenuation profile $P_{A_i}(f, z)$ as both the TRF and its envelope power spectra have similar exponentially decaying characteristics with depth. For a homogeneous medium, $P_A(f, z)$ can be defined by using the AC β (in dB/cm-MHz) as [3], [57]

$$P_A(f, z) = e^{-4\beta f z/8.686} = 10^{-2\beta f z/10}. \tag{3.15}$$

In order to recover the factor $10^{-2\beta f_c z/10}$ at a given depth z and center frequency f_c, the attenuation power spectrum with and without the diffraction effects (i.e., $P_A(f, z) \cdot P_{\widetilde{D}}(f, z)$, and $P_A(f, z)$, respectively) are shown in Fig. 3.7, as calculated by using (3.12) and (3.15). Since the distortion of exponentially decaying attenuation due to diffraction lies in the low frequency region, the less distorted region (e.g., 8 - 20 MHz, beyond the knee point) of the attenuation-diffraction spectrum (blue line) of the TRF stays very near to the attenuation spectrum (red line) at different depths, as illustrated in Fig. 3.7 and thus can be band-pass filtered as

$$P_{H'_{i,e}, BPF}(f, z) \;=\; P_{H'_{i,e}}(f, z) \cdot F(f), \tag{3.16}$$

where

$$F(f) \;=\; \begin{cases} 1, & f_1 \le f \le f_2 \\ 0, & otherwise \end{cases} \tag{3.17}$$

In (3.17), the lower and upper cut-off frequencies f_1 and f_2, respectively, are selected based on the frequency band, where the diffraction effects are supposed to be negligible.

Now, the logarithm of the band-pass filtered power spectrum, $P_{H'_{i,e}, BPF}(f, z)$, can be used for a regression line fitting with frequency to estimate attenuation at the center

frequency (f_c). In Fig. 3.8, the logarithm of the TRF's attenuation-diffraction power spectrum $P_{BPFfit}(f_c, z)$ obtained from the log-linear fit, and of the theoretical center frequency attenuation factor $P_A(f_c, z)(= 10^{-2\beta f_c z/10})$ are shown for different depths and for three AC values. As obvious from Fig. 3.8, the slope of the estimated log power line remains very close to that of the log attenuation line (i.e., $-2\beta f_c z/10$), and thus can be used to estimate the AC value.

After performing the band-pass filtration and log-linear regression, the envelope TRF power spectrum with reduced diffraction effects can be approximated at f_c as

$$P_{H'_{i,e,BPFfit}}(f_c, z) \simeq F_e\big(P_{B'_i}(f_c)\big) \cdot 10^{-2\beta f_c z/10}, \tag{3.18}$$
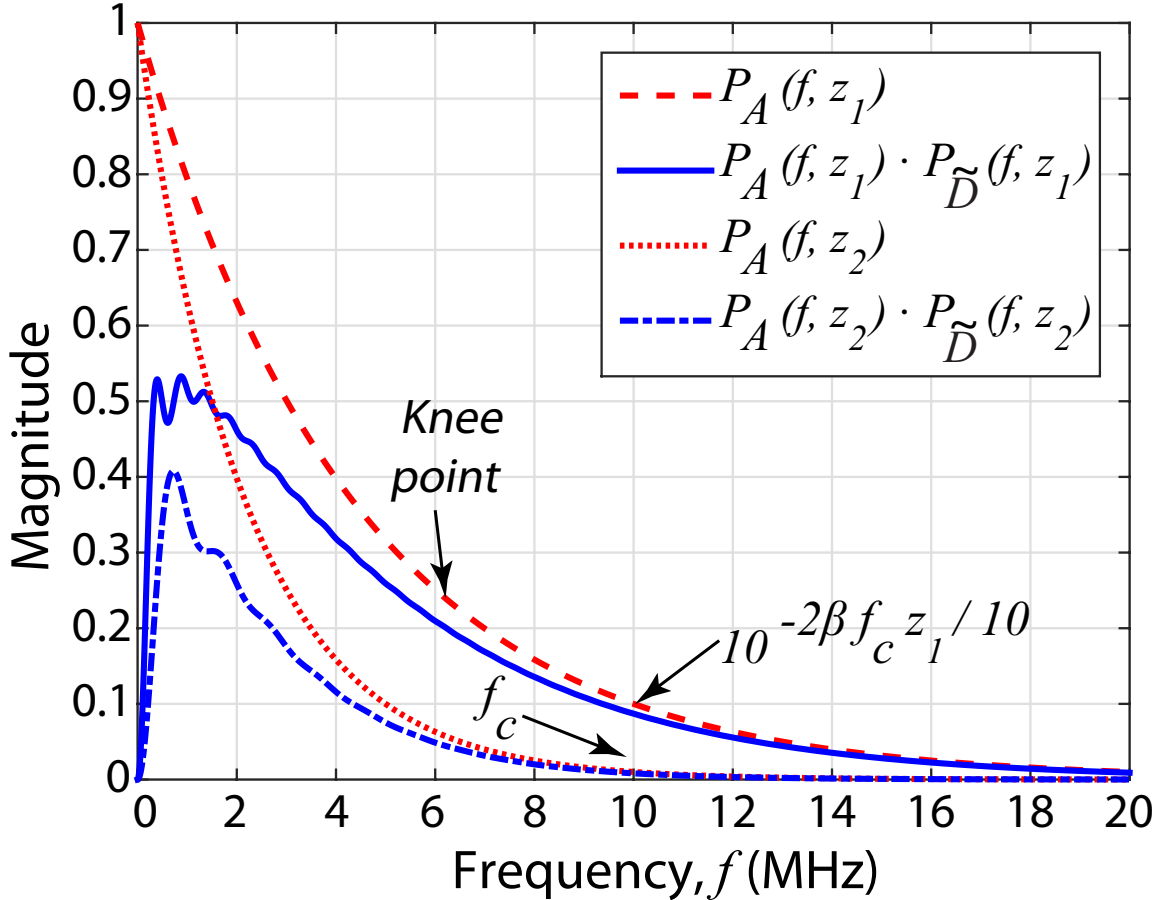
Figure 3.7: The attenuation and diffraction effects on the TRF power spectrum at two depths ($z_1 = 1.0$ cm, $z_2 = 2.0$ cm) and for $\beta = 0.5$ dB/MHz-cm, $f_c = 10$ MHz.

Taking logarithm on both sides of (3.18) yields

$$dBP'(f_c, z) = dBP'_0(f_c) - 2\beta f_c z, \tag{3.19}$$

where $dBP'(f_c, z)$ and $dBP'_0(f_c)$ are decibel representations of $P_{H'_{i,e,BPF}}(f_c, z)$ and $F_e(P_{B'_i}(f_c))$, respectively.

The backscatter coefficient power spectrum $P_B(f)$ of random scatterers has a normal distribution when averaged for the neighborhood within a homogeneous and isotropic ROI [58], and thus its effect can be neutralized by calculating the average TRF power spectrum with depth. The average $\overline{dBP'}(f, z)$ at f_c within a neighborhood can be
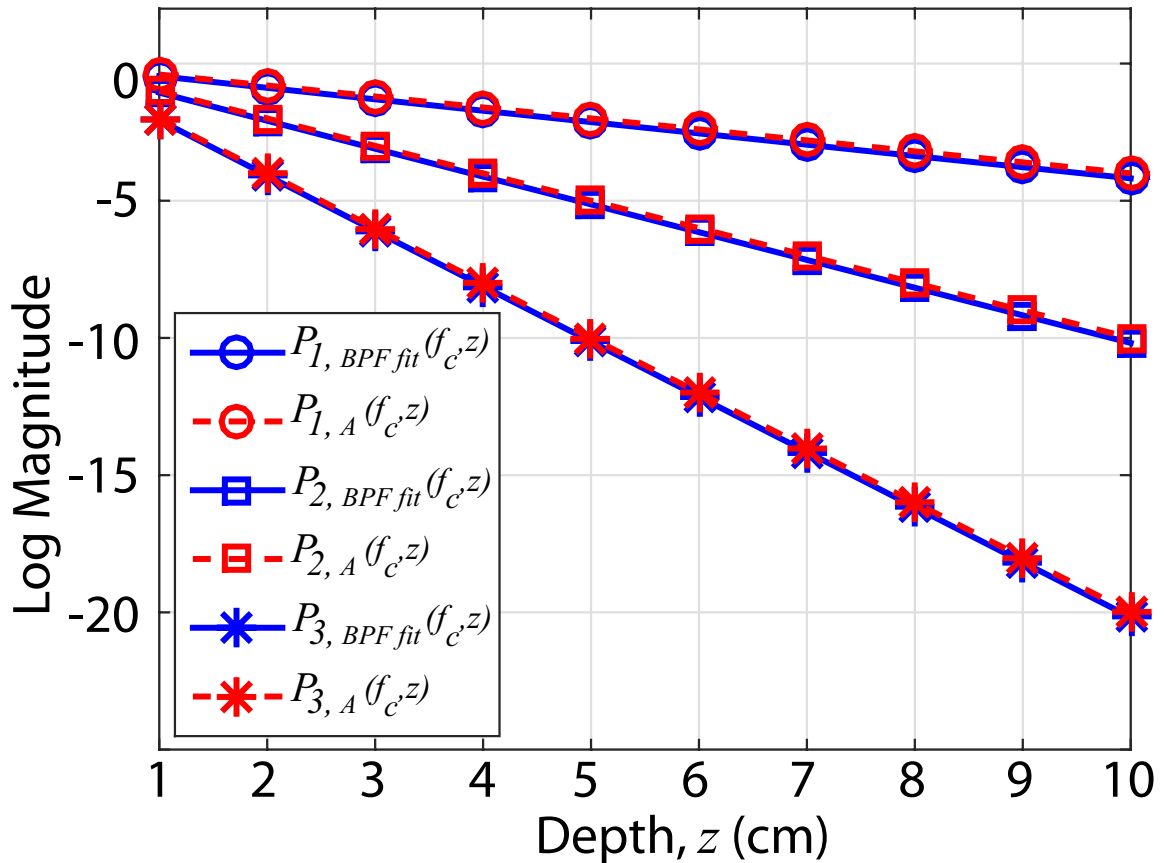
Figure 3.8: The log magnitude of the estimated power $P_{BPFfit}(f_c, z)$ of the bandpass filtered $(8 - 20 \text{ MHz})$ TRF and the center frequency attenuation power content $P_A(f_c, z)$ for different depths and for three AC values $(\beta_1 = 0.2, \beta_2 = 0.5, \text{ and } \beta_3 = 1.0 \text{ dB/MHz-cm})$, where $f_c = 10$ MHz.

written by using (3.19) as

$$\overline{dBP'}(f_c, z) \;=\; dBP'_0 - 2\beta f_c z, \tag{3.20}$$

where dBP'_0 is the decibel representation of the depth-invariant expected value of the backscatter power spectrum function $F_e\big(P_{B'_i}(f_c)\big)$ modeled as a Gaussian random process within the small ROI [3], [58]. The averaging process of $dBP'(f_c, z)$ of the target
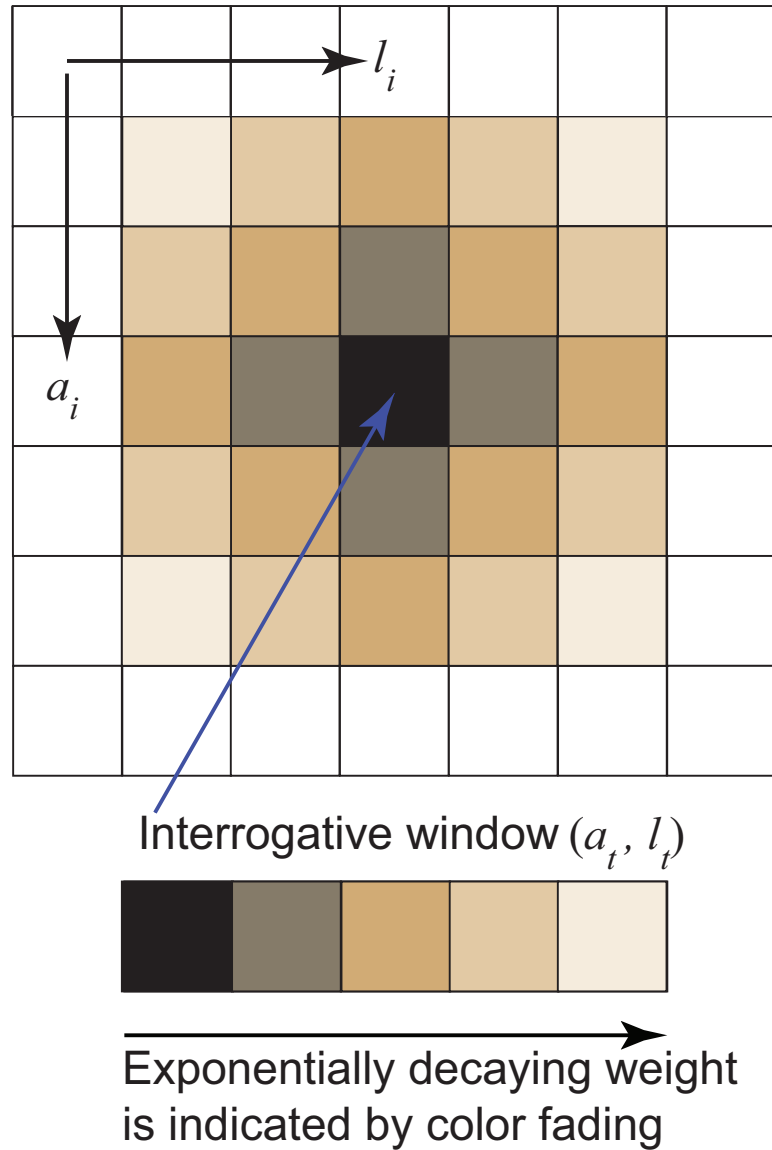
Figure 3.9: Illustration of the weighted exponential contribution of NN in the estimation of effective AC at an investigating point (a_t, l_t).

window is done with the closest neighboring windows having size of $L_a \times L_l$. In order to give more weightage to the target window (at (a_t, l_t)) in the averaging, a 2-D (axial and lateral dimensions) exponential weighting function $w_{t,(a_i,l_i)}$ is utilized (shown in Fig. 3.9). The averaging operation is carried out as

$$
\begin{aligned}
&\overline{dBP'}(f_c, z) \\
&= \frac{\sum\limits_{a_i=a_t-L_a}^{a_t+L_a} \sum\limits_{l_i=l_t-L_l}^{l_t+L_l} w_{t,(a_i,l_i)} \times dBP'_{(a_i,l_i)}(f_c, z)}{\sum\limits_{a_i=a_t-L_a}^{a_t+L_a} \sum\limits_{l_i=l_t-L_l}^{l_t+L_l} w_{t,(a_i,l_i)}},
\end{aligned}
\tag{3.21}
$$

where

$$
w_{t,(a_i,l_i)} = e^{-\left|\frac{(a_i-a_t)}{2}\right| - \left|\frac{(l_i-l_t)}{2}\right|}.
\tag{3.22}
$$

Now, an estimate of AC for the ROI can be calculated from the slope of the fitted line over (3.20) with depth.

It is shown in [48] that the PSF spectrum is depth independent Gaussian function centered at a specific frequency, and thus it is assumed that the attenuation and other system effects are incorporated in the TRF signal as given by (3.3). However, in the estimated average PSF spectra for a particular homogeneous ROI (experimental phantom D, as stated in chapter 4) at different depths, as shown in Fig. 3.10, some variations of the center frequency and magnitude are visible. In Fig. 3.11, by using the estimated power content (with neighborhood technique) of the filtered TRF and PSF envelope signals within the homogeneous ROI, it is shown that the deviation between the attenuation-related depth dependent function (i.e., $-2\beta f_c z$) of power spectrum (in dB) of the TRF-PSF combined and TRF-only is very small, resulted from the depth-dependency of PSF power spectrum (in dB). Methodically, the depth invariant PSF is indicated by the red broken line in Fig. 3.11, and it will be kept as a constant (i.e., intercept) if included in (3.20), as like the backscattering effect $F_e\big(P_{B'_i}(f_c)\big)$. In practical cases, the depth dependent portion shown by the PSF can be considered as a negligible estimation error of the TRF-PSF separation process, which is found to be within $5-10\%$ of the AC value measured by the RFAAE method.

Hence, the AC estimation accuracy from (3.20) can be further improved by adding (3.18) with the bias obtained from the average power of the baseband envelope PSF spectrum ($P_{S'_e}(z)$, proportional to PSF power centered at f_c) as

$$
\begin{aligned}
10log[P_{H'_{i,e,BPFfit},S'_e}(f_c, z)] &= 10log[P_{H'_{i,e,BPFfit}}(f_c, z)] \\
&\quad +10log[P_{S'_e}(z)], \\
\overline{dBP''}(f_c, z) &= dBP''_0 - 2\beta f_c z,
\end{aligned}
\tag{3.23}
$$

where $\overline{dBP''}(f_c, z)$ and dBP''_0 are the modified versions of $\overline{dBP'}(f_c, z)$ and dBP'_0 given in (3.20).
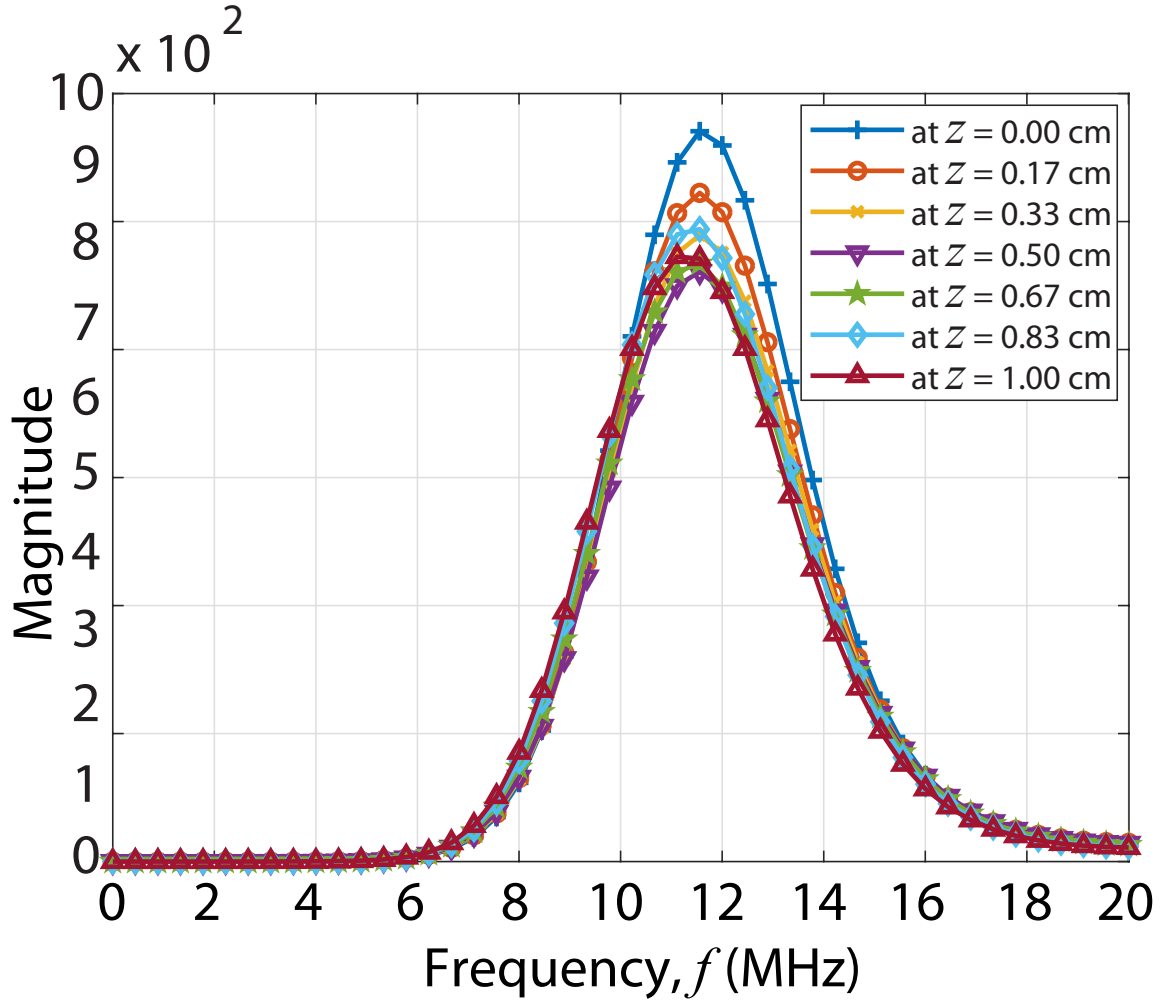
Figure 3.10: The restored average PSF spectra at different depths.

At a given depth z, the linear regression-line centered at f_c over the log power spectrum defined in (3.23) can be expressed as

$$Y(f_c, z) \;=\; I(f_c) - 2\beta f_c z, \tag{3.24}$$

where $Y(f_c, z)$ is the regression-line value at the center frequency f_c in the presence of a linear frequency dependent AC β (dB/cm-MHz). The intercept, $I(f_c)$ corresponds to $Y(f_c, z)$ at $z = 0$.

The impact of taking weighted averaged logarithmic intensities (i.e., from line segments $i-5$ to $i+5$) on the AC determination of the i-th interrogative scan line segment using (3.24), is shown in Fig. 3.12. Here, the plots are shown for the 1 cm RF scan line
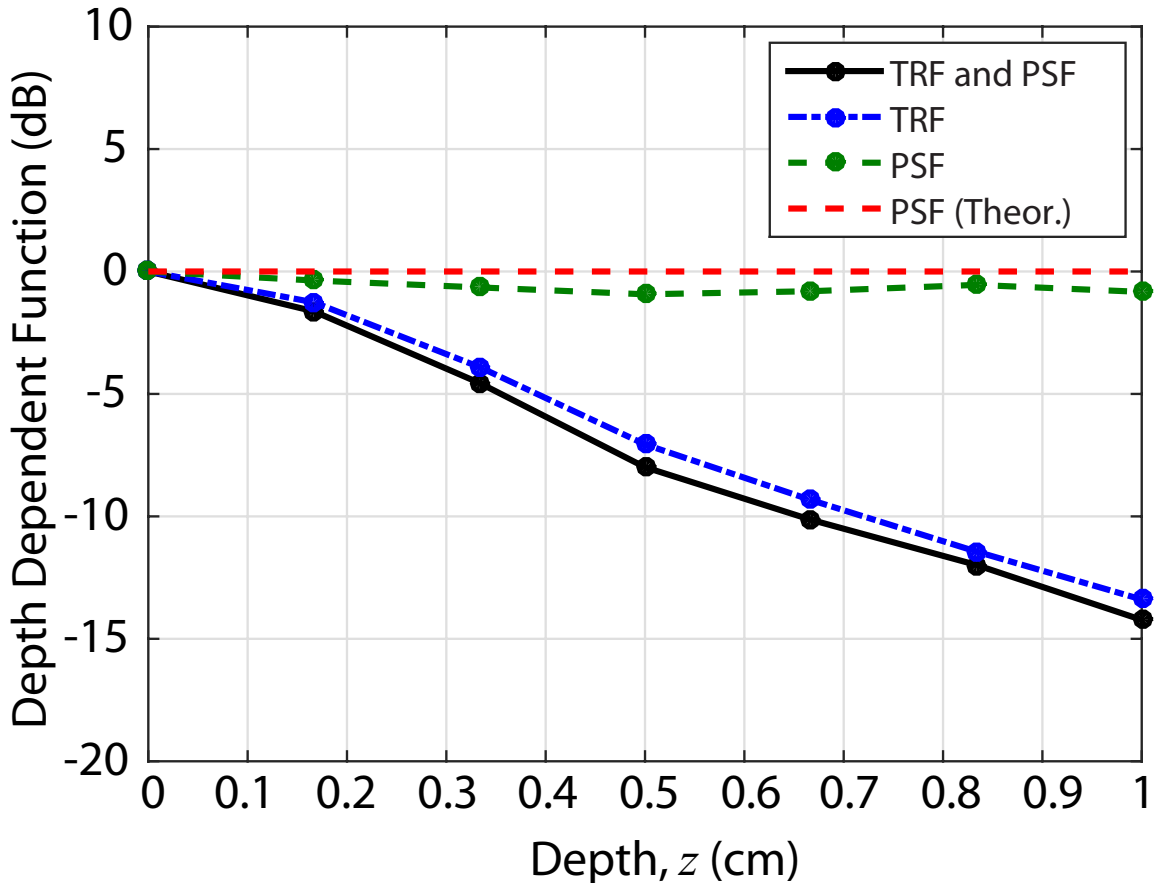
Figure 3.11: The depth dependent functions calculated from the decibel power spectrum of TRF, PSF and combined TRF-PSF.

segments of a type D experimental phantom (details are given in Table 4.1 of chapter 4) partitioned into seven 1-D blocks with 50% overlapping in the axial direction. In fact, the proposed RFAAE method becomes more robust by using the neighborhood $(L_a \times L_l)$ technique given in (3.21), as the i-th weighted average plot ($L_a = L_l = 5$) is almost aligned with the fitted straight line and is more linear in nature than any of the instantaneous logarithmic intensity plots (i.e., $i - 5$ to $i + 5$) without using the neighborhood ($L_a = L_l = 0$). The obtained AC value (0.74 dB/cm-MHz) from the i-th fitted line is also very close the actual value (0.70 dB/cm-MHz). This fact can be taken as an evidence of proper system effects mitigation in AC estimation in the absence of reference data.
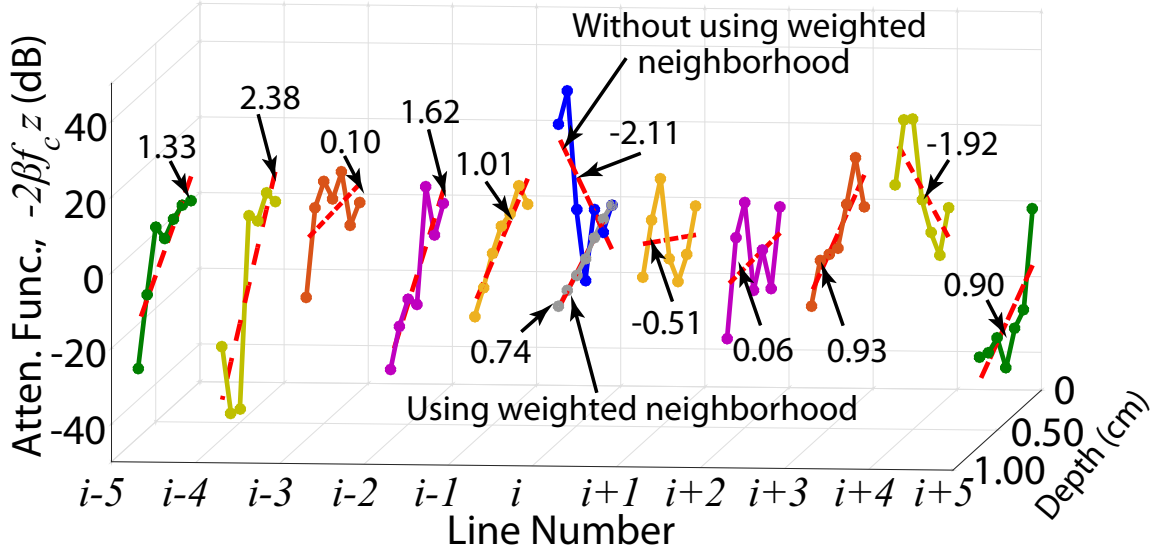
Figure 3.12: The regression lines ($i-5$ to $i+5$) of instantaneous logarithmic intensities, and the regression line (i) of weighted average logarithmic intensity along with the corresponding intensity (in dB) plots for the proposed RFAAE method. Here, the estimated AC (i.e., β in dB/cm-MHz) value from each of regression lines is shown.

Now, the comparison of linearity of the attenuation function (i.e., $-2\beta f_c z$) with depth obtained by proposed RFAAE method with that of the reference-based SNAAE method [6] is shown in Fig. 3.13 for the i-th scan line segment (mentioned in the previous paragraph). The measured ACs of the arbitrary ROI by using the neigh-
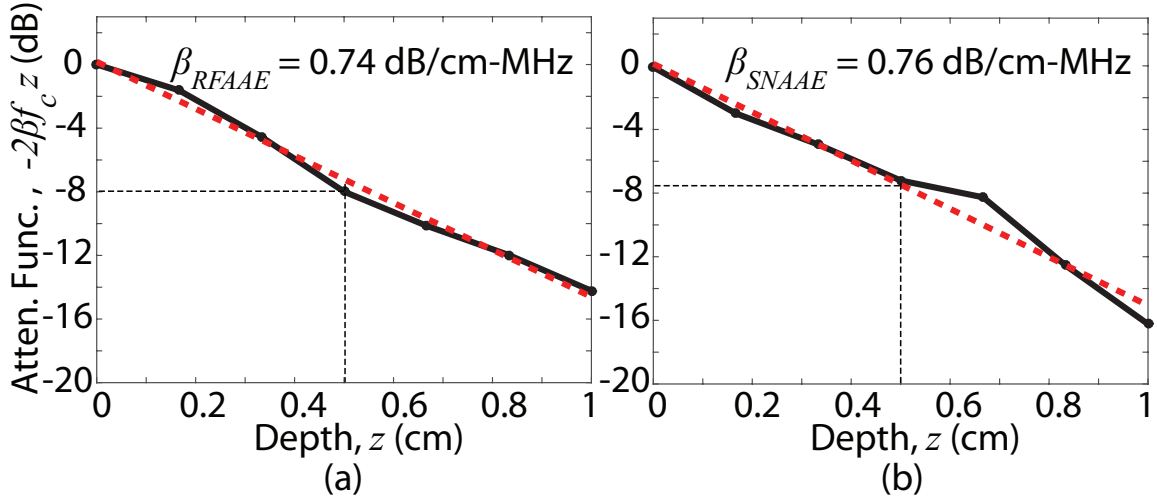
Figure 3.13: The attenuation (i.e., $-2\beta f_c z$) function (solid line) of the log power spectrum along the regression line (broken line) using the same RF data for (a) RFAAE method and (b) conventional SNAAE method.

borhood weighted averaging based RFAAE and SNAAE methods are very close (i.e., 0.74 and 0.76 dB/cm-MHz, respectively). However, the estimate of the attenuation function (i.e., $-2\beta f_c z$) with depth provided by the RFAAE method (using (3.24)) is more linear (better line fit) than that obtained from the SNAAE method, as evident from Fig. 3.13. Therefore, the proposed RFAAE method is expected to perform well in a realistic environment.

Chapter 4

Experimental Results and Discussion

The main focus of this chapter is to assess the viability of the proposed RFAAE algorithm under different clinical conditions. For this purpose, the experiments performed on the tissue-mimicking (TM) phantoms, *in vivo* human breast and liver data are discussed in detail here. The performance of this new estimator is analyzed comparing its results with those obtained by the conventional reference-based AC estimation methods (spectral shift [5], spectral difference [7], hybrid [8], SNAAE and SCAAE [6]).

4.1   Analysis of RF Data

To apply the proposed RFAAE and other reference-based spectral domain AC estimation methods, the homogeneous ROI of the RF data is subdivided into a number of overlapping, rectangular 2-D blocks. The 2-D block size is required to be optimized in such a way that the frequency and spatial resolutions are sufficient for correct estimation of AC. Regarding these conditions, full width at half maximum (FWHM) of the RF power spectrum [5] is used as a benchmark for assessing the dimensions of the block. However, for the purposes of estimating AC at a higher spatial resolution, like the proposed RFAAE method, the block size is chosen to be 4.70 mm (axial) × 3.13

mm (lateral) for the spectral difference, spectral shift, and hybrid methods. Based on the findings in the literature [5], [7], [8], 50% overlapping is used in axial direction, but one scan line (i.e., around 10% overlapping) in lateral directions. Every block consists of three windows, and the overlap and length of the windows in the axial direction are 50% and 2.35 mm (i.e., 15λ), respectively, as demonstrated in Fig. 4.1. The power spectrum within the data block at a particular depth is calculated axially by an averaging of the fast Fourier transform of the 1-D gated (i.e., Hamming window) windows. The Hamming window is utilized here to reduce the effects of spectral leakage [59]. Each of the blocks has 10 scan lines as suggested by its lateral dimension. Therefore, the averaged power spectrum of the entire block of the ROI is measured from 10×3 number of 1-D axial windows for obtaining an accurate estimate of the spectral information.
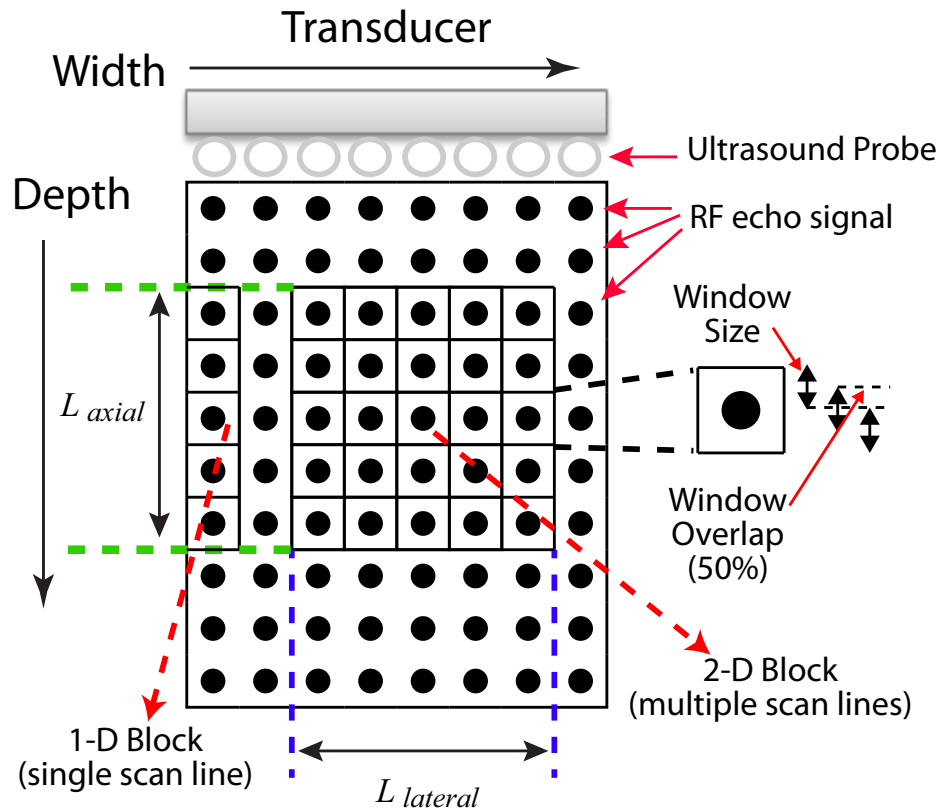
Figure 4.1: Illustration of the blocks in a RF frame.

Fundamentally, for the RFAAE algorithm, 1-D blocks of length 4.70 mm (axial) are used, which have only one scan line. Additionally, at the higher spatial resolution, the AC estimation becomes better with the neighborhood utilization within the ROI [6]. In this approach, 10 neighboring scan line segments (in lateral direction) are used along with the scan line segment of the interrogated 1-D block for the exponentially weighted average and, therefore, result in an effective lateral width of 3.13 mm.

The length of the linear line fitting window over the logarithmic center frequency component of the ROI blocks, is taken as half of the axial length of that RF data (i.e., 2 cm for a 4×4 cm^2 RF data). This is a common standard that is followed in estimating the local AC using the RFAAE and other discussed reference-based methods.

4.2 Simulation Results

To validate the usefulness of the proposed methodology in the presence of diffraction effects, realistic RF data generated by the state-of-the-art ultrasound simulation program Field II [53] were utilized. A homogeneous phantom ($40 \times 10 \times 40$ mm^3 cube) was made for the simulation, where the scatterer number density is 15 per resolution cell. The backscatterers in the phantom are randomly distributed, and with a Gaussian distributed scattering amplitude. The phantom was scanned with a 192 element linear array transducer, and 64 active elements were used for receiving and transmitting with a Hanning apodization. The rectangular elements of the transducer are 0.3 mm in width (azimuthal direction), 5 mm in length (elevation direction), and with a kerf (i.e., lateral distance between the adjacent elements) of 0.015 mm. The transducer was excited with 2 cycles of a 10 MHz Hanning windowed sinusoid. The sampling frequency was 40 MHz and the focal distance from the top surface of the phantom was set at 20 mm. The simulated backscattered RF data were acquired with 128 scan-lines.

The B-mode images of the phantom and the two types of RF datasets obtained are shown in Figs. 4.2(a)-4.2(c) along with their amplitude-depth plot for the lateral center line. The RF data of Fig. 4.2(b) and Fig. 4.2(c) were simulated by transmitting the pulse into the homogeneous phantom medium with two different AC values. In both

the cases, the diffraction effects are present due to beam focusing. For the RF datasets, as represented in Fig. 4.2(b) and Fig. 4.2(c), the frequency independent attenuation values were set to 5 dB/cm and 7.5 dB/cm, respectively, and the frequency dependent attenuation values (i.e., AC values) were set to 0.5 dB/cm-MHz and 0.75 dB/cm-MHz, respectively,. Three ROIs X, Y, and Z each with a dimension of 10×10 mm^2 are chosen from the two RF datasets for obtaining the AC estimates.

The average estimates of the normalized center frequency components of the depth dependent function (DDF) at three different depths of the ROIs are measured by using (3.2), (3.13), and (3.23), as shown in Figs. 4.2(d)- 4.2(f), 4.2(g)- 4.2(i), and 4.2(j)- 4.2(l), respectively. Here, an estimate of the changed center frequency value of the RF datasets is obtained from the restored PSF spectrum rather than using the provided value. The equations given in (3.2) and (3.13) are used to estimate the AC values without and with PSF-TRF separation in the absence of the diffraction related band-pass filtering, as illustrated in 4.2(g)- 4.2(i) and 4.2(j)- 4.2(l), respectively. For the ROIs (X, Y, and, Z) of the homogeneously attenuating medium with an AC of 0.5 dB/cm-MHz, the ultimate average AC values (β_{avg}) estimated from the slopes of the regression lines by using (3.23) are 0.55, 0.50, and 0.49 dB/cm-MHz, and for the attenuating medium with an AC of 0.75 dB/cm-MHz, these values (β'_{avg}) are 0.75, 0.72, and 0.78 dB/cm-MHz, as shown in 4.2(j)- 4.2(l). It can be observed that these AC estimates are close to the actual values after the PSF separtion and diffraction minimization procedures. The diffraction effects are known to distort the regions that are before and after the focal zones along the depth, thus the estimated AC values are supposed to be underestimated and overestimated in that regions, respectively [55]. As suggested by the demonstrated results, the proposed RFAAE technique is shown to be capable of determining the accurate AC values in those regions.
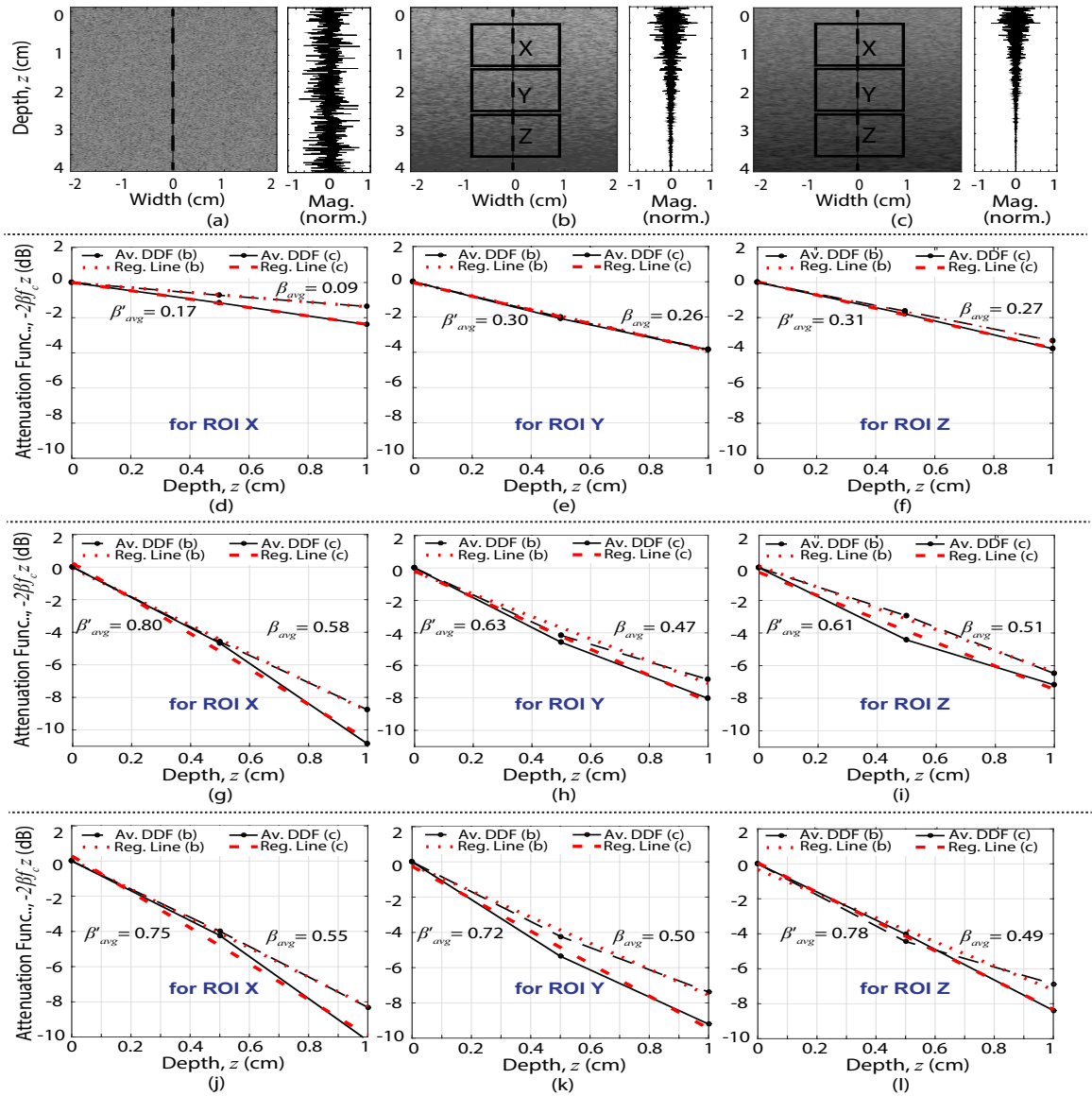
Figure 4.2: B-mode images and estimated AC values of the simulated phantom for two different sets of attenuation. (a) A homogeneous phantom, (b) the attenuated B-mode image with AC = 0.5 dB/cm-MHz, (c) the attenuated B-mode image with AC = 0.75 dB/cm-MHz, with RF intensity (normalized) plots along the indicated broken lines, respectively; and (d)-(f), (g)-(i), and (j)-(l) the average depth dependent functions (DDF), and the corresponding regression lines for the three ROIs (X, Y, and Z, indicated in (b) and (c)), calculated by using (3.2), (3.13), and (3.23), respectively.

Table 4.1: Properties of the four types of TM phantoms used in the study

Property	Type A	Type B	Type C	Type D
Size	4×4 cm^2	4×4 cm^2	5×4 cm^2	4×4 cm^2
Inc. type	—	—	Spherical	Cylindrical
Inc. size	—	—	0.70 cm (Diameter)	1.67 cm (Diameter)
Inc. Distance (from upper side)	—	—	4 cm	2 cm
AC (dB/cm-MHz)	0.50 (Bg.)	0.70 (Bg.)	0.50 (Bg.), 0.95 (Inc.)	0.50 (Bg.), 0.70 (Inc.)

* Inc. (inclusion), Bg. (background)
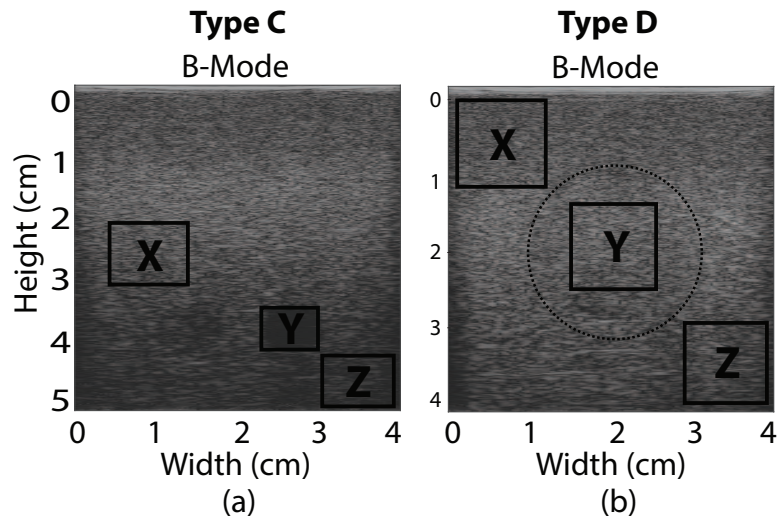
Figure 4.3: B-mode images of the TM phantom type C and D with inclusions (properties are given at Table 4.1). ROIs X and Z are from the background and ROIs Y from the inclusion areas, with dimension of 1.00×1.00 cm^2 each (except ROI Y of 0.70×0.70 cm^2 in type C).

4.3   TM Phantom Experiments

4.3.1   Data Collection

To validate the proposed technique, four types (A, B, C, and D) of CIRS (Computerized Imaging Reference Systems, Inc., Norfolk, VA, USA), TM phantom datasets were used. In Table 4.1, all the relevant information of these TM phantom datasets provided by the manufacturer are incorporated. Among these phantoms, type A and B are

Figure 4.4: SonixTOUCH ultrasound Research instrument used at BUET Medical Center.

homogeneous in nature with AC of 0.5 and 0.7 dB/cm-MHz, respectively. The ROIs of heterogeneous type C and D phantoms are chosen from these phantoms are termed as X, Y, and Z, as depicted in Fig. 4.3. Among these ROIs, X and Z were taken from homogeneous background with dimension of 1.0×1.0 cm^2 and AC of 0.5 dB/cm-MHz. ROI Y was taken from the inclusion part of the phantoms having AC of 0.95 and 0.70 dB/cm-MHz for type C and D phantoms, respectively. All the segments of the TM phantoms were constructed from hydrogel-based Zerdine, having an acoustic velocity of 1540 m/s. The raw data were recorded in .rf format on a SonixTOUCH ultrasound Research instrument (Ultrasonix Medical Corp., Richmond, BC, Canada) (shown in Fig. 4.4) at the Medical Center of Bangladesh University of Engineering and Technology (BUET), Dhaka, Bangladesh. The L14-5/38 linear array transducer was used here with a center frequency of 10 MHz, 65% bandwidth at FWHM of the power spectrum, sampling frequency of 40 MHz, and geometric focus at 2 cm away from the probe surface. During the data acquisition, no TGC was used.

4.3.2 Results and Discussion

The AC map calculated from the RF data of type A and type B phantoms, by using the RFAAE and the traditional reference-based AC estimation schemes, are shown in Figs. 4.5(b)-(i) and 4.6(b)-(i) along with the B-mode images in Figs. 4.5(a) and 4.6(a). Because of the requirement of a homogeneous reference phantom dataset with identical system parameters as of the sample, type A and type B phantoms were used alternatively to each other by the mentioned reference-based methods. For the spectral difference, spectral shift, and hybrid methods, simple spectral averaging of overlapping windows is accomplished in both the directions within the 2-D blocks. However, the variances within the AC figures produced by the spectral shift and hybrid techniques are comparatively higher, which are clearly observable from Figs. 4.5(c)-4.5(d), and 4.6(c)-4.6(d). The spectral difference method tends to provide lower variances, but the estimated AC values are gradually overestimated and underestimated with depth after the focal zones, as shown in 4.5(b) and 4.6(b), respectively. On the other hand, the reference-based SCAAE and SNAAE methods utilizing the 1-D blocks with exponen-
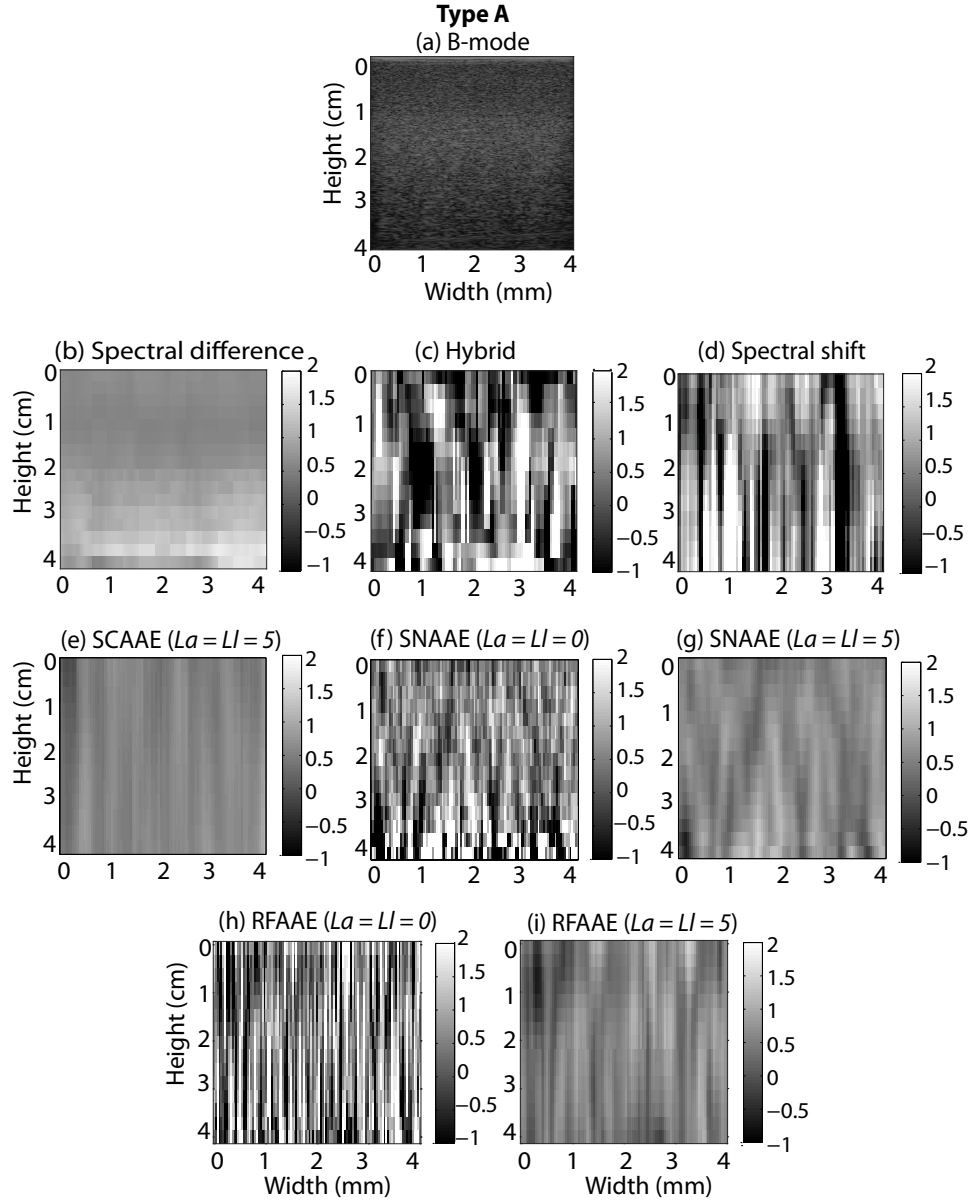
Figure 4.5: Figure (a) represents the B-mode image, and the corresponding AC mapping ((b), (c), (d), (e), (f), (g), (h), and (i)) are obtained by employing the spectral difference, hybrid, spectral shift, SCAAE (for $L_a = L_l = 5$), SNAAE (for $L_a = L_l = 0$), SNAAE (for $L_a = L_l = 5$), proposed RFAAE (for $L_a = L_l = 0$), and RFAAE (for $L_a = L_l = 5$) methods, respectively, for the TM phantom type A (The actual AC value is mentioned in Table 4.1). Except the RFAAE method, for other reference-based methods, type B phantom is used as reference here.
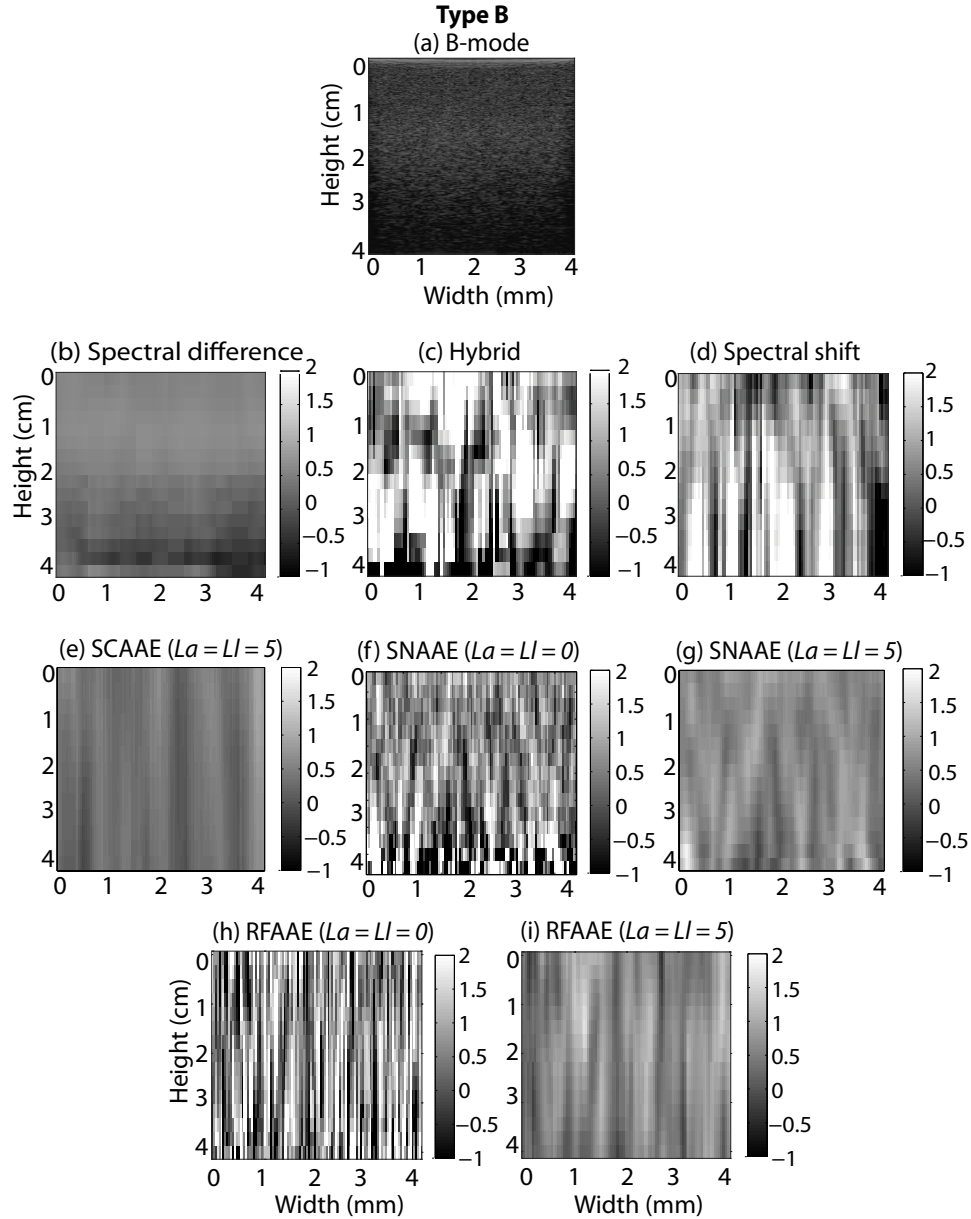
Figure 4.6: Figure (a) represents the B-mode image, and the corresponding AC mapping ((b), (c), (d), (e), (f), (g), (h), and (i)) are obtained by employing the spectral difference, hybrid, spectral shift, SCAAE (for $L_a = L_l = 5$), SNAAE (for $L_a = L_l = 0$), SNAAE (for $L_a = L_l = 5$), proposed RFAAE (for $L_a = L_l = 0$), and RFAAE (for $L_a = L_l = 5$) methods, respectively, for the TM phantom type B (The actual AC value is mentioned in Table 4.1). Except the RFAAE method, for other reference-based methods, type A phantom is used as reference here.
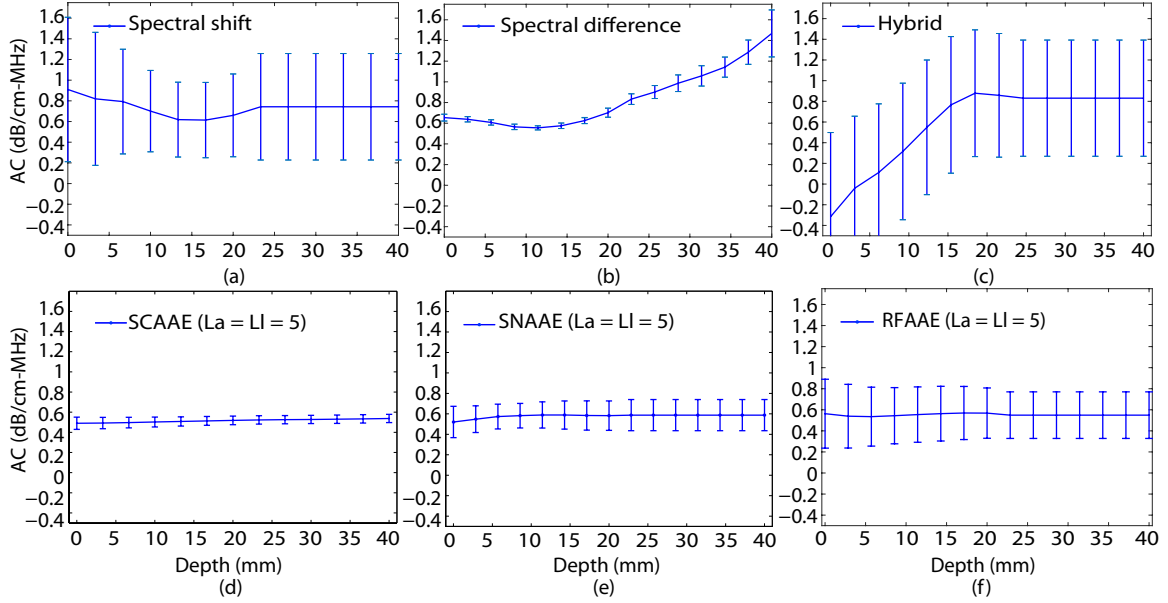
Figure 4.7: Average AC estimates with SD of type A TM phantom at different axial depths obtained by the discussed reference-based (spectral shift (a), spectral difference (b), hybrid (c), SCAAE (for $L_a = L_l = 5$) (d), SNAAE (for $L_a = L_l = 5$) (e)), and the proposed RFAAE (for $L_a = L_l = 5$) (f) methods. Here, the actual AC value of type A is 0.5 dB/cm-MHz.

tially weighted neighborhood ($L_a \times L_l$) resulted in AC values within acceptable limits, as evident from Figs. 4.5(e), 4.5(g), and 4.6(e), 4.6(g). By using the idea of 1-D block with the integrated neighborhood, the extent of the smoothed AC map obtained by the RFAAE method is similar to the SNAAE and SCAAE methods without compromising the accuracy of the AC value at a given depth, as shown in Figs. 4.5(i) and 4.6(i). The idea of using the neighborhood ($L_a = L_l = 5$) was previously introduced for variance reduction, but its impact gets much emphasized for the proposed RFAAE method in the absence of reference data, as obvious from the larger variances in Figs. 4.5(h) and 4.6(h) compared to Figs. 4.5(f) and 4.6(f).

Figs. 4.7 and 4.8 are presented to show the exactness and variability of the AC estimates at different axial depths from the probe surface within type A and B phantoms, respectively. Here, the spectral difference method resulted in variable estimated
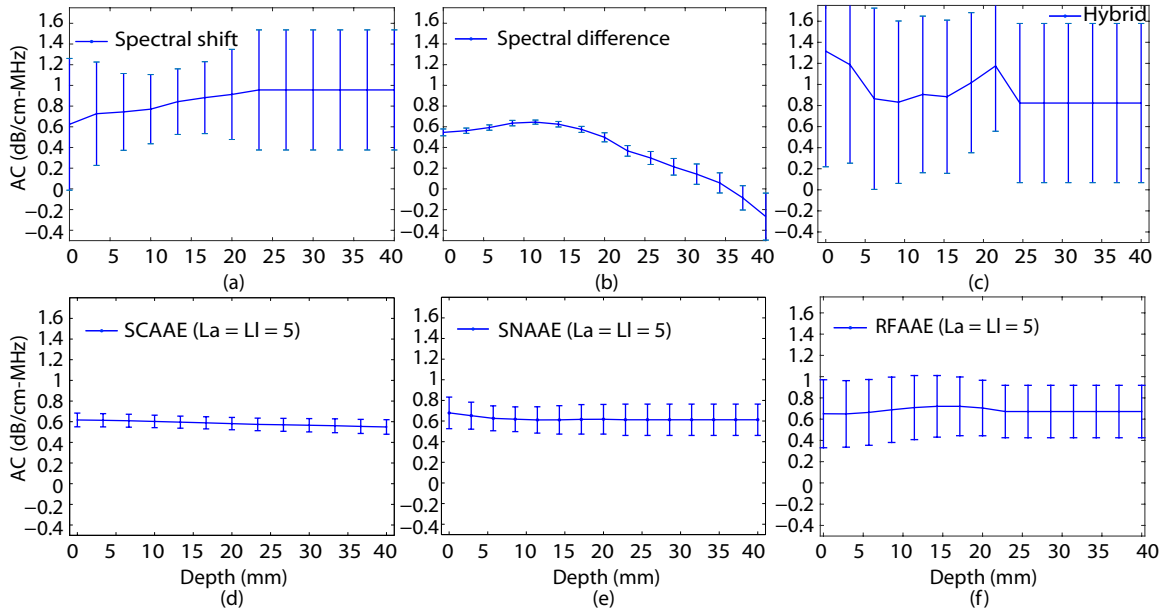
Figure 4.8: Average AC estimates with SD of type B TM phantom at different axial depths obtained by the discussed reference-based (spectral shift (a), spectral difference (b), hybrid (c), SCAAE (for $L_a = L_l = 5$) (d), SNAAE (for $L_a = L_l = 5$) (e)), and the proposed RFAAE (for $L_a = L_l = 5$) (f) methods. Here, the actual AC value of type B is 0.7 dB/cm-MHz.

average value of the AC along the depth as shown in Figs. 4.7(b) and 4.8(b), although the variances are very small in lateral direction. The average AC estimates generated by the spectral shift and the hybrid methods have moderate variations with depth, but the estimates near the ultrasound probe surface have higher deviations as evident from Figs. 4.7(a), 4.8(a), and 4.7(c), 4.8(c), respectively. The SD of the later method is also relatively higher towards the lateral dimension. However, the neighborhood-based ($L_a = L_l = 5$) SNAAE and SCAAE methods resulted in almost accurate average AC values at all depths, as obvious from the lines that are nearly parallel to depth axis in Figs. 4.7 and 4.8 (at the second row). The SCAAE method has been found to provide the lowest variance in lateral direction among all the methods, at the cost of putting more weightage to the neighborhood than the SNAAE method [6]. Actually, for AC calculation, SCAAE method does not rely on the direct utilization of the instantaneous

cross-correlation based spectral downshift. In this method, an approximate diffraction correction is made in the sample AC estimates by using a well-specified reference phantom. Considering these facts, the new RFAAE method is capable of providing approximately similar average AC estimates along the depth with moderate SD in the lateral direction, as obvious from Figs. 4.7(f) and 4.8(f), without using any reference data.
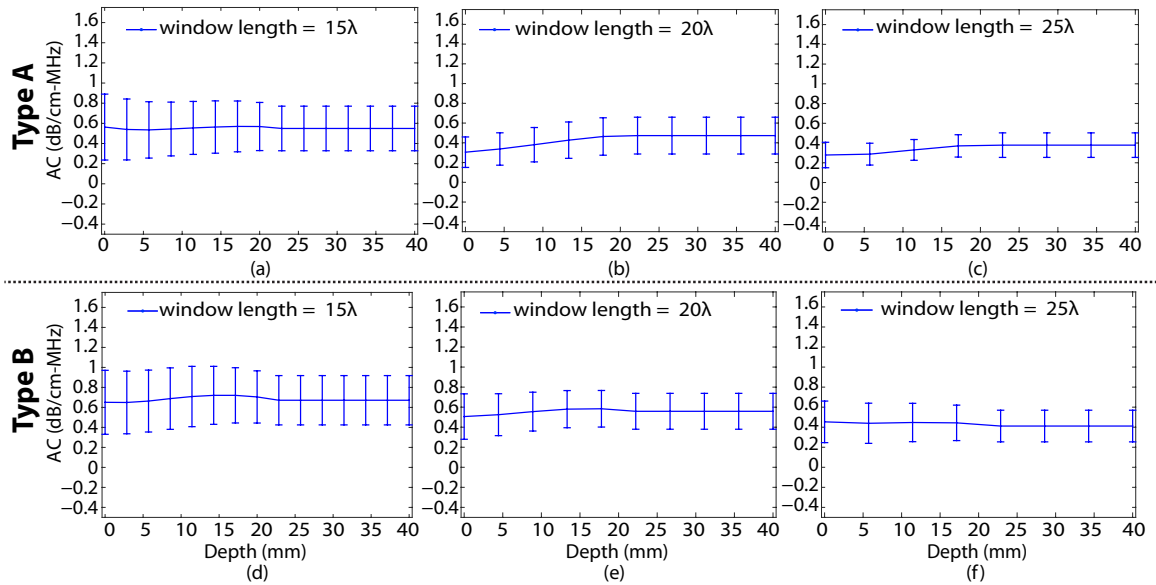
Figure 4.9: Average AC estimates with SD of type A ((a)-(c)) and type B ((d)-(f)) TM phantom datasets at different axial depths by using the proposed RFAAE (for $L_a = L_l = 5$) method with window lengths of 15λ, 20λ, and 25λ. Here, the actual AC values of type A and type B are 0.5 and 0.7 dB/cm-MHz, respectively.

In Fig. 4.9, the average and SD values of AC estimates at different axial depths within type A and type B TM phantom datasets are compared for three window lengths (i.e., 15λ, 20λ, and 25λ). Here, the minimum window length (i.e., 15λ) is chosen based on the FWHM criterion in order to get stable block power spectra [5]. Visually assessing the plots for type A (Figs. 4.9(a)-4.9(c)) and type B (Figs. 4.9(d)-4.9(f)) TM phantom datasets, it is observed that the decrease in the SD values is small with the increase of window length. Moreover, the deviations of the average AC estimates from the actual

values become significant at the higher window lengths. By considering the spatial resolution of AC mapping, the optimum window length was selected to be 15λ for the proposed RFAAE (for $L_a = L_l = 5$) method.

Table 4.2: Type C: Average AC estimates with SD (inside brackets) by the proposed RFAAE and other reference-based methods

Methods	ROI X	ROI Y	ROI Z
	(dB/cm-MHz)	(dB/cm-MHz)	(dB/cm-MHz)
Spectral shift [5]	0.56 ($\pm$0.34)	0.79 ($\pm$0.72)	0.51 ($\pm$0.25)
Spectral difference [7]	0.80 ($\pm$0.39)	0.76 ($\pm$0.82)	0.73 ($\pm$0.37)
Hybrid [8]	0.56 ($\pm$0.42)	0.71 ($\pm$0.37)	0.45 ($\pm$0.34)
SNAAE (L_a=L_l=0) [6]	0.60 ($\pm$0.16)	0.22 ($\pm$0.29)	0.49 ($\pm$0.14)
SNAAE (L_a=L_l=5) [6]	0.48 ($\pm$0.29)	1.00 ($\pm$0.27)	0.51 ($\pm$0.25)
SCAAE (L_a=L_l=5) [6]	0.54 ($\pm$0.11)	0.91 ($\pm$0.10)	0.48 ($\pm$0.09)
RFAAE (L_a=L_l=5)	0.48 ($\pm$0.24)	0.90 ($\pm$0.25)	0.51 ($\pm$0.26)

Actual AC values (dB/cm-MHz): 0.50 (ROI X), 0.95 (ROI Y), 0.50 (ROI Z)

Next, AC estimates given in Tables 4.2 and 4.3 are obtained from the chosen ROIs (shown in Fig. 4.3) of the type C and D TM phantoms, by using the RFAAE and other above-mentioned methods. Here, type B phantom is selected for providing the reference ROI of the same size and at the same depth for the reference-based methods. In case of type C phantom, some deviations are shown by the spectral difference, spectral shift and hybrid methods from the actual AC values. The SD values are also large especially for the inclusion ROI Y. On the other hand, the spectral shift and hybrid methods resulted in close estimate of actual AC values for the ROIs of data D, excluding the ROI Y for spectral shift where the estimated average value is relatively high. The spectral difference method becomes unsuccessful for the ROIs of data C and D, as apparent from the average and SD values. The SNAAE and SCAAE methods depend highly on the neighborhood for the accuracy and coherence of the AC estimates at the ROIs for both types of phantoms, in addition to utilizing the reference

Table 4.3: Type D: Average AC estimates with SD (inside brackets) by the proposed RFAAE and other reference-based methods

Methods	ROI X (dB/cm-MHz)	ROI Y (dB/cm-MHz)	ROI Z (dB/cm-MHz)
Spectral shift [5]	0.43 ($\pm$0.24)	0.87 ($\pm$0.22)	0.34 ($\pm$0.23)
Spectral difference [7]	0.35 ($\pm$0.60)	0.42 ($\pm$0.46)	0.47 ($\pm$0.39)
Hybrid [8]	0.51 ($\pm$0.08)	0.68 ($\pm$0.16)	0.52 ($\pm$0.07)
SNAAE ($L_a=L_l=0$) [6]	0.54 ($\pm$0.25)	0.37 ($\pm$0.23)	0.37 ($\pm$0.39)
SNAAE ($L_a=L_l=5$) [6]	0.52 ($\pm$0.30)	0.66 ($\pm$0.23)	0.44 ($\pm$0.27)
SCAAE ($L_a=L_l=5$) [6]	0.48 ($\pm$0.08)	0.72 ($\pm$0.11)	0.47 ($\pm$0.09)
RFAAE ($L_a=L_l=5$)	0.47 ($\pm$0.22)	0.74 ($\pm$0.16)	0.53 ($\pm$0.24)

Actual AC values (dB/cm-MHz): 0.50 (ROI X), 0.70 (ROI Y), 0.50 (ROI Z)

data for system effects compensation. Methodically, RFAAE is used to measure the center frequency component of the envelope power spectrum within a neighborhood of the RF data as like the SNAAE, except that no reference is used here. Therefore, the results acquired by the RFAAE, have similar average and SD values as like the SNAAE method, which are within 10% of the actual AC values.

4.4 *In vivo* Experiments

4.4.1 Data Collection

For accuracy assessment of the AC estimates in soft biological tissues (e.g., breast, liver), a comparative analysis of the newly developed RFAAE and other reference-based methods is further conducted involving human participants. In order to accomplish the task, three female participants (participant-I/age: 48 years, participant-II/age: 40 years, and participant-III/age: 58 years; mean: 48.67, SD: 9.02 years) were chosen for the *in vivo* breast RF datasets and seventeen male-female participants (14 participants

(normal liver)/age range: 23-60, mean: 35.18, SD: 13.78 years, and 3 participants (fatty liver)/age range: 27-51, mean: 42.67, SD: 13.58 years) were selected for the *in vivo* liver RF datasets. These datasets were acquired in .rf format using a SonixTOUCH ultrasound Research machine (Ultrasonix Medical Corporation, Richmond BC, Canada), by an expert radiologist at BUET Medical Center, Dhaka, Bangladesh. To be specific, a L14-5/38 linear transducer (operating frequency: 10 MHz, bandwidth: 65% at FWHM of power spectrum, sampling frequency: 40 MHz, and focus: 2 cm) and a C5-2/60 convex transducer (operating frequency: 3.3 MHz, bandwidth: 75.76% at FWHM of power spectrum, sampling frequency: 20 MHz, and focus: 5 cm) were applied for acquiring the breast and liver RF data, respectively, as shown in Fig. 4.10. For the whole procedure, permission was taken from the institutional review board (IRB), and the participants have granted research analysis on the datasets. The dimension of the *in*

(a)   (b)

Figure 4.10: (a) The L14-5/38 Linear Transducer, and (b) The C5-2/60 Convex Transducer of the sonixTOUCH ultrasound research device.

vivo breast and liver RF acoustic images were 4×4 cm^2 and 16×6 cm^2, respectively. The block related parameters were kept similar as in the case of AC estimation of the TM phantoms. During the data acquisition, no TGC was used.
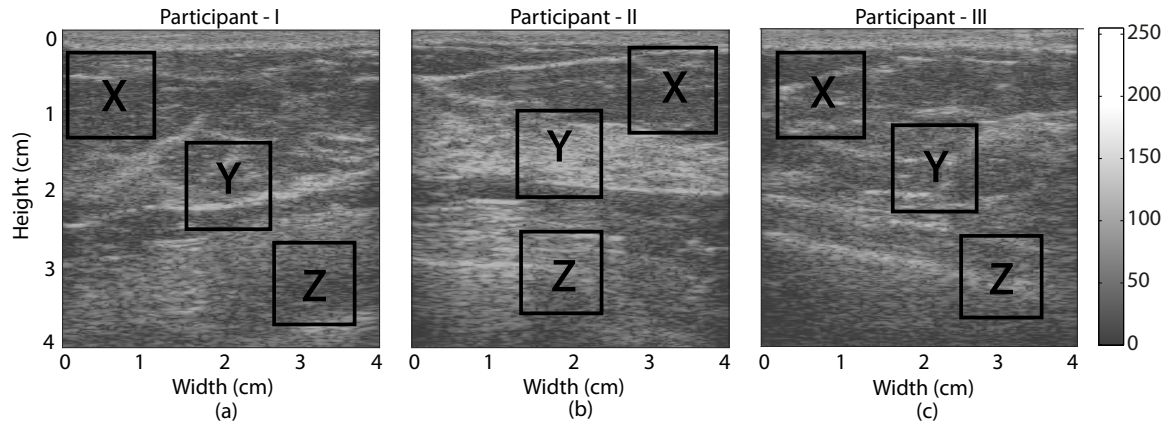
Figure 4.11: *In vivo* human breast RF data in the form of B-mode images collected from (a) participant-I, (b) participant-II, and (c) participant-III. ROIs X, Y, and Z are homogeneous regions of 1.00×1.00 cm^2 each.
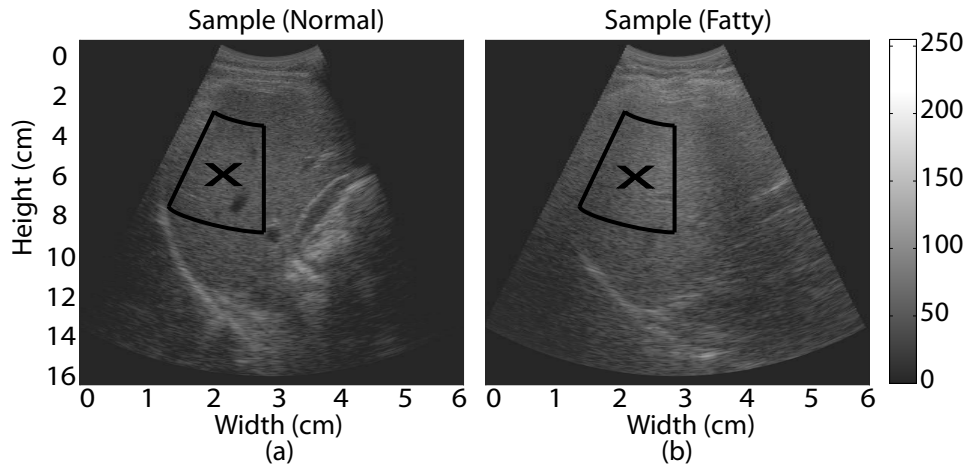
Figure 4.12: *In vivo* human liver RF data in the form of B-mode images collected from (a) sample (Normal Liver), (b) sample (Fatty Liver). ROIs X are homogeneous regions of 7.00×2.00 cm^2 each.

In Figs. 4.11 and 4.12, the B-mode images of the sample breast and liver data, respectively, are illustrated along with the ROIs. For the breast datasets, three ROIs

(X, Y, and Z) were chosen at different depths with approximate homogeneous regions of 1×1 cm^2. In case of the liver datasets, one large ROI (X) is obtained from the greater part of the sample liver, having dimension of 7×2 cm^2. The calculated AC values along with SD for breast and liver datasets using the particular techniques are given in Tables 4.5–4.7, and Tables 4.8, 4.9, respectively. To implement the reference-based traditional methods, a previously used homogeneous reference TM phantom of type A is applied for the breast data of the research participants. For the liver data, a homogeneous TM phantom with AC value of 0.5 dB/cm-MHz and dimension of 16×6 cm^2 is used as reference, where the phantom RF data were recorded by the convex transducer under the same conditions involved in the sample data collection.

4.4.2   Results and Discussion

Table 4.4: Literature-reported AC values in soft tissue

Tissue types	AC (dB/cm-MHz)	Reference
Soft tissue	0.2–0.5	[60]
Soft tissue (Average)	0.60	[61]
Soft tissue (Average)	0.54	[62]
Fat	0.60	[61]
Fat	0.48	[62]
Fat	0.35	[63]
Fat	0.44	[64]
Normal Liver (Average)	0.49–0.59	[65], [66]
Fatty Liver (Average)	0.57–0.83	[65], [66]

The acoustic images of heterogeneous soft tissues consist of various homogeneous regions like muscles, skin, tendons, ligaments, fascia, fat, fibrous tissue, nerves and blood vessels. The literature-reported AC values for different types of tissue are enlisted

in Table 4.4, which are needed to assess the robustness of the AC estimation techniques.

Table 4.5: participant-I (Breast Dataset): Average AC estimates with SD (inside brackets) by the proposed RFAAE and other reference-based methods

Methods	ROI X	ROI Y	ROI Z
	(dB/cm-MHz)	(dB/cm-MHz)	(dB/cm-MHz)
Spectral shift [5]	0.79 ($\pm$0.51)	0.98 ($\pm$0.64)	0.42 ($\pm$0.24)
Spectral difference [7]	0.57 ($\pm$0.57)	0.93 ($\pm$0.64)	0.47 ($\pm$0.36)
Hybrid [8]	0.49 ($\pm$0.08)	0.50 ($\pm$0.08)	0.51 ($\pm$0.06)
SNAAE ($L_a=L_l=0$) [6]	0.52 ($\pm$0.06)	0.49 ($\pm$0.12)	0.49 ($\pm$0.28)
SNAAE ($L_a=L_l=5$) [6]	0.46 ($\pm$0.24)	0.58 ($\pm$0.30)	0.53 ($\pm$0.34)
SCAAE ($L_a=L_l=5$) [6]	0.43 ($\pm$0.10)	0.57 ($\pm$0.10)	0.50 ($\pm$0.03)
RFAAE ($L_a=L_l=5$)	0.38 ($\pm$0.26)	0.42 ($\pm$0.24)	0.55 ($\pm$0.29)

Table 4.6: participant-II (Breast Dataset): Average AC estimates with SD (inside brackets) by the proposed RFAAE and other reference-based methods

Methods	ROI X	ROI Y	ROI Z
	(dB/cm-MHz)	(dB/cm-MHz)	(dB/cm-MHz)
Spectral shift [5]	0.14 ($\pm$0.12)	0.47 ($\pm$0.21)	0.38 ($\pm$0.28)
Spectral difference [7]	0.40 ($\pm$0.57)	0.76 ($\pm$0.49)	0.26 ($\pm$0.33)
Hybrid [8]	0.48 ($\pm$0.08)	0.49 ($\pm$0.06)	0.47 ($\pm$0.09)
SNAAE ($L_a=L_l=0$) [6]	0.52 ($\pm$0.45)	0.66 ($\pm$0.31)	0.36 ($\pm$0.27)
SNAAE ($L_a=L_l=5$) [6]	0.48 ($\pm$0.33)	0.46 ($\pm$0.26)	0.47 ($\pm$0.20)
SCAAE ($L_a=L_l=5$) [6]	0.45 ($\pm$0.08)	0.50 ($\pm$0.06)	0.53 ($\pm$0.11)
RFAAE ($L_a=L_l=5$)	0.48 ($\pm$0.24)	0.40 ($\pm$0.21)	0.41 ($\pm$0.21)

From the results shown in Tables 4.5–4.7 for the ROIs of breast datasets, it can be noticed that the average AC values provided by the spectral difference and spectral

Table 4.7: participant-III (Breast Dataset): Average AC estimates with SD (inside brackets) by the proposed RFAAE and other reference-based methods

Methods	ROI X	ROI Y	ROI Z
	(dB/cm-MHz)	(dB/cm-MHz)	(dB/cm-MHz)
Spectral shift [5]	0.17 ($\pm$0.13)	0.68 ($\pm$0.44)	0.60 ($\pm$0.34)
Spectral difference [7]	0.59 ($\pm$0.54)	0.62 ($\pm$0.52)	0.18 ($\pm$0.35)
Hybrid [8]	0.50 ($\pm$0.05)	0.51 ($\pm$0.08)	0.46 ($\pm$0.07)
SNAAE ($L_a=L_l=0$) [6]	0.59 ($\pm$0.38)	0.45 ($\pm$0.27)	0.70 ($\pm$0.23)
SNAAE ($L_a=L_l=5$) [6]	0.35 ($\pm$0.20)	0.62 ($\pm$0.34)	0.53 ($\pm$0.14)
SCAAE ($L_a=L_l=5$) [6]	0.45 ($\pm$0.05)	0.55 ($\pm$0.13)	0.50 ($\pm$0.10)
RFAAE ($L_a=L_l=5$)	0.37 ($\pm$0.14)	0.49 ($\pm$0.21)	0.46 ($\pm$0.17)

shift methods in most cases are not within the desired range (i.e., 0.35–0.60 dB/cm-MHz for fatty and soft tissue, as given in Table 4.4). The hybrid method tends to be invariant to some extent in all the breast ROI cases with AC values close to 0.50 dB/cm-MHz, and the SD values are also low due to the equally-weighted average of the spectra in the axial and lateral dimensions. In cases of the SNAAE method, the variances are much higher than that for the SCAAE method because of the relatively higher susceptibility to the backscatter variations in the breast tissues. The AC values estimated by the proposed RFAAE algorithm are reasonable (i.e., ranging from 0.37 to 0.55 dB/cm-MHz), as given in Tables 4.5–4.7. However, considering the variation of tissue microstructure characteristics and the absence of reference data, this technique resulted in moderate SD values for all the ROIs mentioned in Tables 4.5–4.7.

In case of liver, mainly two categories of tissue (i.e., normal and fatty) were employed for getting the AC estimates enlisted in Tables 4.8 and 4.9. Because of the homogeneity of liver tissue, as shown in Fig. 4.12, a close estimate of the actual AC value can be obtained from the measured RF data. Considering the reported values for liver tissues in Table 4.4, the AC estimates obtained between 0.2 and 1.0 dB/cm-MHz (outside this range is considered unrealistic) by using the reference-based and the

Table 4.8: Average (Normal Liver - 14 Datasets): Average AC estimates with SD (inside brackets) by the proposed RFAAE and other reference-based methods

Methods	ROI
	(dB/cm-MHz)
SNAAE ($L_a=L_l=5$) [6]	0.48 ($\pm$0.11)
SCAAE ($L_a=L_l=5$) [6]	0.53 ($\pm$0.07)
RFAAE ($L_a=L_l=5$)	0.55 ($\pm$0.21)

Table 4.9: Average (Fatty Liver - 3 Datasets): Average AC estimates with SD (inside brackets) by the proposed RFAAE and other reference-based methods

Methods	ROI
	(dB/cm-MHz)
SNAAE ($L_a=L_l=5$) [6]	0.61 ($\pm$0.12)
SCAAE ($L_a=L_l=5$) [6]	0.53 ($\pm$0.06)
RFAAE ($L_a=L_l=5$)	0.61 ($\pm$0.20)

proposed RFAAE methods are employed for the average and SD calculation. As representatives of the reference-based methods, the SNAAE and SCAAE methods tend to produce fair results for normal liver cases compared to the reported values of 0.49–0.59 dB/cm-MHz given in Table 4.4. But the SCAAE method leads to inaccurate average AC value for fatty liver cases (reported values: 0.57–0.83 dB/cm-MHz, as listed in Table 4.4), implying the improper system effects compensation caused by using the reference phantom with AC value of 0.5 dB/cm-MHz. On the other hand, the new RFAAE technique proves to be effective in both the cases as shown by the results (0.55 and 0.61 dB/cm-MHz for the normal and fatty livers, respectively). However, for the new method, the SD of the AC estimates is relatively higher within the ROIs X than for the reference-based methods.

After the inspection of all the results provided in this Chapter, it can be inferred

that the derived RFAAE (with $L_a = L_l = 5$) technique is able to estimate acceptable AC values, without the use of reference data that is compulsory in other methods for canceling the diffraction and other undesired system effects. Adding to this point, the method is also computationally efficient for estimating AC from 1-D blocks resulting higher resolution with the help of the neighborhood technique within the sample ROI.

Chapter 5

Conclusion, Limitation and Future Scope

5.1 Conclusion

A novel reference-free average AC estimation method has been presented in this thesis, which is based on the envelope TRF and envelope PSF power spectra models of the RF signal. With a non-reference based ultrasound system-related effects (e.g., beam diffraction, transmit pulse) reduction process, the proposed RFAAE method is capable of providing reasonable estimates of AC. In order to separate the PSF from the TRF containing the attenuation function, an improved cepstral liftering process for the RF signal is proposed in the RFAAE technique. In the power spectra modeling, the high-pass spectral characteristic of the diffraction function is utilized for estimating the center frequency component of the exponential attenuation function. Under the continuity assumption of attenuation within the block surroundings, AC estimates are obtained from the slope of the regression line that is fitted to the exponentially weighted logarithmic power content of the neighborhood blocks with depth. Further, to cope with the random tissue backscattering effects in the AC estimation of a homogeneous ROI, inclusion of the neighboring blocks is necessary in the weighted averaging process together with the target block. The results obtained by the proposed RFAAE

method from the experimental tests done in this thesis, are in good agreement with the actual and other literature-reported AC values. Different from the traditional ones, the proposed RFAAE method with weighted neighborhood utilization of the 1-D blocks, resulted in reasonable AC estimates of the sample data at a higher spatial resolution. The estimates are also free from the external biases that are usually introduced by the dissimilar properties (i.e., effective frequency) of sample and reference data. Furthermore, the RFAAE method may be effective in measuring the mean AC values of those data for which the reference data are not available.

5.2 Limitation and Future Scope

The main concentration of this research work is set on the accurate determination of AC as a clinical diagnostic parameter within a small homogeneous tissue segment in the absence of any reference data. The moderate AC variance obtained in the proposed RFAAE method suggests that intensive studies are required on the random tissue structures. Although the vulnerability of the AC estimates to the system effects (i.e., diffraction and backscattering effects) is counteracted effectively by the participation of the band-pass filtering and neighbourhood averaging, better estimation can be achieved by the data based adaptive utilization of the signal processing tools. The potential future works are focused on improving the estimation consistency of the RFAAE technique and using this AC estimator with other features for tissue characterization.

Bibliography

[1] J. M. Blackledge, *Quantitative Coherent Imaging: Theory, Methods and Some Applications.* Elsevier Academic Press, 2012.

[2] Y. Labyed and T. A. Bigelow, "A theoretical comparison of attenuation measurement techniques from backscattered ultrasound echoes," *J. Acoust. Soc. Am.*, vol. 129, no. 4, pp. 2316–2324, 2011.

[3] S. W. Flax, N. J. Pelc, G. H. Glover, F. D. Gutmann, and M. McLachlan, "Spectral characterization and attenuation measurements in ultrasound," *Ultrason. Imaging*, vol. 5, no. 2, pp. 95–116, 1983.

[4] B. Knipp, J. Zagzebski, T. Wilson, F. Dong, and E. Madsen, "Attenuation and backscatter estimation using video signal analysis applied to B-mode images," *Ultrason. Imaging*, vol. 19, no. 3, pp. 221–233, 1997.

[5] H. Kim and T. Varghese, "Attenuation estimation using spectral cross-correlation," *IEEE Trans. Ultrason. Ferroelectr. Freq. Control*, vol. 54, no. 3, p. 510, 2007.

[6] M. K. Hasan, M. A. Hussain, S. R. Ara, S. Y. Lee, and S. K. Alam, "Using nearest neighbors for accurate estimation of ultrasonic attenuation in the spectral domain," *IEEE Trans. Ultrason. Ferroelectr. Freq. Control*, vol. 60, no. 6, pp. 1098–1114, 2013.

[7] L. X. Yao, J. A. Zagzebski, and E. L. Madsen, "Backscatter coefficient measurements using a reference phantom to extract depth-dependent instrumentation factors," *Ultrason. Imaging*, vol. 12, no. 1, pp. 58–70, 1990.

[8] H. Kim and T. Varghese, "Hybrid spectral domain method for attenuation slope estimation," *Ultrasound Med. Biol.*, vol. 34, no. 11, pp. 1808–1819, 2008.

[9] Z. Klimonda, M. Postema, A. Nowicki, and J. Litniewski, "Tissue attenuation estimation by mean frequency downshift and bandwidth limitation," *IEEE Trans. Ultrason. Ferroelectr. Freq. Control*, vol. 63, no. 8, pp. 1107–1115, 2016.

[10] K. Dines and A. Kak, "Ultrasonic attenuation tomography of soft tissues," *Ultrason. Imaging*, vol. 1, no. 1, pp. 16–33, 1979.

[11] P. D. Lui, M. K. Terris, J. E. McNeal, and T. A. Stamey, "Original articles: Prostate cancer: Indications for ultrasound guided transition zone biopsies in the detection of prostate cancer," *J. Urol.*, vol. 153, no. 3, pp. 1000–1003, 1995.

[12] J. Mamou, M. L. Oelze, W. D. O'Brien Jr, and J. F. Zachary, "Identifying ultrasonic scattering sites from three-dimensional impedance maps," *J. Acoust. Soc. Am.*, vol. 117, no. 1, pp. 413–423, 2005.

[13] M. L. Oelze and W. D. O'Brien Jr, "Frequency-dependent attenuation-compensation functions for ultrasonic signals backscattered from random media," *J. Acoust. Soc. Am.*, vol. 111, no. 5, pp. 2308–2319, 2002.

[14] G. Treece, R. Prager, and A. Gee, "Ultrasound attenuation measurement in the presence of scatterer variation for reduction of shadowing and enhancement," *IEEE Trans. Ultrason. Ferroelectr. Freq. Control*, vol. 52, no. 12, pp. 2346–2360, 2005.

[15] G. Berger, P. Laugier, J. Thalabard, and J. Perrin, "Global breast attenuation: Control group and benign breast diseases," *Ultrason. Imaging*, vol. 12, no. 1, pp. 47–57, 1990.

[16] B. Oosterveld, J. Thijssen, P. Hartman, R. Romijn, and G. Rosenbusch, "Ultrasound attenuation and texture analysis of diffuse liver disease: methods and preliminary results," *Phys. Med. Biol.*, vol. 36, no. 8, p. 1039, 1991.

[17] T. Wilson, Q. Chen, J. A. Zagzebski, T. Varghese, and L. VanMiddlesworth, "Initial clinical experience imaging scatterer size and strain in thyroid nodules," *J. Ultrasound Med.*, vol. 25, no. 8, pp. 1021–1029, 2006.

[18] P. He and J. F. Greenleaf, "Application of stochastic analysis to ultrasonic echoes: estimation of attenuation and tissue heterogeneity from peaks of echo envelope," *J. Acoust. Soc. Am.*, vol. 79, no. 2, pp. 526–534, 1986.

[19] H. S. Jang, T. K. Song, and S. B. Park, "Ultrasound attenuation estimation in soft tissue using the entropy difference of pulsed echoes between two adjacent envelope segments," *Ultrason. Imaging*, vol. 10, no. 4, pp. 248–264, 1988.

[20] R. Kuc and M. Schwartz, "Estimating the acoustic attenuation coefficient slope for liver from reflected ultrasound signals," *IEEE Trans. Sonics Ultrason.*, vol. 26, no. 5, pp. 353–361, 1979.

[21] M. Insana, J. Zagzebski, and E. Madsen, "Improvements in the spectral difference method for measuring ultrasonic attenuation," *Ultrason. Imaging*, vol. 5, no. 4, pp. 331–345, 1983.

[22] K. J. Parker, R. M. Lerner, and R. C. Waag, "Comparison of techniques for in vivo attenuation measurements," *IEEE Trans. Biomed. Eng.*, vol. 35, no. 12, pp. 1064–1068, 1988.

[23] M. Fink, F. Hottier, and J. Cardoso, "Ultrasonic signal processing for in vivo attenuation measurement: Short time Fourier analysis," *Ultrason. Imaging*, vol. 5, no. 2, pp. 117–135, 1983.

[24] K. J. Parker and R. C. Waag, "Measurement of ultrasonic attenuation within regions selected from B-scan images," *IEEE Trans. Biomed. Eng.*, no. 8, pp. 431–437, 1983.

[25] P. Narayana and J. Ophir, "The measurement of attenuation in nonlinearly atten-
uating media by the zero crossing method," *Ultrasound Med. Biol.*, vol. 10, no. 6,
pp. 715–718, 1984.

[26] D. E. Sosnovik, S. L. Baldwin, S. H. Lewis, M. R. Holland, and J. G. Miller,
"Transmural variation of myocardial attenuation measured with a clinical imager,"
Ultrasound Med. Biol., vol. 27, no. 12, pp. 1643–1650, 2001.

[27] E. Omari, H. Lee, and T. Varghese, "Theoretical and phantom based investigation
of the impact of sound speed and backscatter variations on attenuation slope
estimation," *Ultrasonics*, vol. 51, no. 6, pp. 758–767, 2011.

[28] H. Tu, J. Zagzebski, and Q. Chen, "Attenuation estimations using envelope echo
data: Analysis and simulations," *Ultrasound Med. Biol.*, vol. 32, no. 3, pp. 377–
386, 2006.

[29] A. Kurjak, "Ultrasound scanning–Prof. Ian Donald (1910–1987)," *Eur. J. Obstet.
gynecol. Reprod. Biol.*, vol. 90, no. 2, pp. 187–189, 2000.

[30] N. M. Tole, H. Ostensen, W. H. Organization, *et al.*, "Basic physics of ultrasonic
imaging," 2005.

[31] G. H. Mostbeck, *Duplex and Color Doppler Imaging of the Venous System: With
27 Tables.* Springer Science & Business Media, 2004.

[32] F. Calliada, R. Campani, O. Bottinelli, A. Bozzini, and M. G. Sommaruga, "Ul-
trasound contrast agents: basic principles," *Eur. Radiol.*, vol. 27, pp. S157–S160,
1998.

[33] J. A. Jensen, J. Mathorne, T. Gravesen, and B. Stage, "Deconvolution of in vivo
ultrasound B-mode images," *Ultrason. Imaging*, vol. 15, no. 2, pp. 122–133, 1993.

[34] S. J. Norton and M. Linzer, "Ultrasonic reflectivity imaging in three dimensions:
exact inverse scattering solutions for plane, cylindrical, and spherical apertures,"
IEEE Trans. Biomed. Eng., no. 2, pp. 202–220, 1981.

[35] N. Zhao, A. Basarab, D. Kouamé, and J.-Y. Tourneret, "Joint segmentation and deconvolution of ultrasound images using a hierarchical Bayesian model based on generalized gaussian priors," *IEEE Trans. Image Process.*, vol. 25, no. 8, pp. 3736–3750, 2016.

[36] O. V. Michailovich and D. Adam, "A novel approach to the 2-D blind deconvolution problem in medical ultrasound," *IEEE Trans. Med. Imag.*, vol. 24, no. 1, pp. 86–104, 2005.

[37] J. A. Jensen, "A model for the propagation and scattering of ultrasound in tissue," *J. Acoust. Soc. Am.*, vol. 89, no. 1, pp. 182–190, 1991.

[38] O. Mattausch and O. Goksel, "Image-based reconstruction of tissue scatterers using beam steering for ultrasound simulation," *IEEE Trans. Med. Imag.*, vol. 37, no. 3, pp. 767–780, 2018.

[39] H. Gao, H. F. Choi, P. Claus, S. Boonen, S. Jaecques, G. H. Van Lenthe, G. Van der Perre, W. Lauriks, and J. D'hooge, "A fast convolution-based methodology to simulate 2-dd/3-d cardiac ultrasound images," *IEEE Trans. Ultrason. Ferroelectr. Freq. Control*, vol. 56, no. 2, pp. 404–409, 2009.

[40] M. Alessandrini, S. Maggio, J. Porée, L. De Marchi, N. Speciale, E. Franceschini, O. Bernard, and O. Basset, "A restoration framework for ultrasonic tissue characterization," *IEEE Trans. Ultrason. Ferroelectr. Freq. Control*, vol. 58, no. 11, 2011.

[41] J. Ng, R. Prager, N. Kingsbury, G. Treece, and A. Gee, "Wavelet restoration of medical pulse-echo ultrasound images in an EM framework," *IEEE Trans. Ultrason. Ferroelectr. Freq. Control*, vol. 54, no. 3, 2007.

[42] P. Narayana, J. Ophir, and N. Maklad, "The attenuation of ultrasound in biological fluids," *J. Acoust. Soc. Am.*, vol. 76, no. 1, pp. 1–4, 1984.

[43] U. R. Abeyratne, A. P. Petropulu, and J. M. Reid, "Higher order spectra based deconvolution of ultrasound images," *IEEE Trans. Ultrason. Ferroelectr. Freq. Control*, vol. 42, no. 6, pp. 1064–1075, 1995.

[44] C. Yu, C. Zhang, and L. Xie, "A blind deconvolution approach to ultrasound imaging," *IEEE Trans. Ultrason. Ferroelectr. Freq. Control*, vol. 59, no. 2, 2012.

[45] O. Michailovich and A. Tannenbaum, "Blind deconvolution of medical ultrasound images: A parametric inverse filtering approach," *IEEE Trans. Image Process.*, vol. 16, no. 12, pp. 3005–3019, 2007.

[46] J. A. Jensen and S. Leeman, "Nonparametric estimation of ultrasound pulses," *IEEE Trans. Biomed. Eng.*, vol. 41, no. 10, pp. 929–936, 1994.

[47] T. Taxt, "Comparison of cepstrum-based methods for radial blind deconvolution of ultrasound images," *IEEE Trans. Ultrason. Ferroelectr. Freq. Control*, vol. 44, no. 3, pp. 666–674, 1997.

[48] K. A. Wear, "A Gaussian framework for modeling effects of frequency-dependent attenuation, frequency-dependent scattering, and gating," *IEEE Trans. Ultrason. Ferroelectr. Freq. Control*, vol. 49, no. 11, pp. 1572–1582, 2002.

[49] C. Yu, C. Zhang, and L. Xie, "An envelope signal based deconvolution algorithm for ultrasound imaging," *Signal processing*, vol. 92, no. 3, pp. 793–800, 2012.

[50] S. L. Hahn, *Hilbert Transforms in Signal Processing*. Artech House, Inc., Boston, 1996.

[51] S. M. Schimmel, *Theory of modulation frequency analysis and modulation filtering, with applications to hearing devices*. Citeseer, 2007, vol. 68, no. 07.

[52] P. H. Rogers and A. L. Van Buren, "An exact expression for the Lommel-diffraction correction integral," *J. Acoust. Soc. Am.*, vol. 55, no. 4, pp. 724–728, 1974.

[53] J. A. Jensen, "Simulation of advanced ultrasound systems using Field II," in *Proc. IEEE Int. Symp. Biomed. Imag., Nano Macro*, Apr. 2004, pp. 636–639.

[54] J. A. Jensen, "Linear description of ultrasound imaging systems," *Notes for the International Summer School on Advanced Ultrasound Imaging, Technical University of Denmark*, vol. 5, p. 54, 1999.

[55] W. A. Verhoef, M. J. Cloostermans, and J. M. Thijssen, "Diffraction and dispersion effects on the estimation of ultrasound attenuation and velocity in biological tissues," *IEEE Trans. Biomed. Eng.*, no. 7, pp. 521–529, 1985.

[56] M. A. Fink and J. F. Cardoso, "Diffraction effects in pulse-echo measurement," *IEEE Trans. Sonics Ultrason.*, vol. 31, no. 4, pp. 313–329, 1984.

[57] R. Kuc, "Bounds on estimating the acoustic attenuation of small tissue regions from reflected ultrasound," *Proc. IEEE*, vol. 73, no. 7, pp. 1159–1168, 1985.

[58] K. Samimi and T. Varghese, "Lower bound on estimation variance of the ultrasonic attenuation coefficient using the spectral-difference reference-phantom method," *Ultrason. Imaging*, vol. 39, no. 3, pp. 151–171, 2017.

[59] A. V. Oppenheim and R. W. Schafer, *Digital Signal Processing*. Prentice Hall, Inc., Englewood Cliffs, New Jersey, 1975.

[60] P. N. Wells and H. D. Liang, "Medical ultrasound: imaging of soft tissue strain and elasticity," *J. R. Soc. Interface*, vol. 8, no. 64, pp. 1521–1549, 2011.

[61] P. N. Wells, "Ultrasonic imaging of the human body," *Rep. Prog. Phys.*, vol. 62, no. 5, p. 671, 1999.

[62] M. O. Culjat, D. Goldenberg, P. Tewari, and R. S. Singh, "A review of tissue substitutes for ultrasound imaging," *Ultrasound Med. Biol.*, vol. 36, no. 6, pp. 861–873, 2010.

[63] L. Landini and R. Sarnelli, "Evaluation of the attenuation coefficients in normal and pathological breast tissue," *Med. Biol. Eng. Comput.*, vol. 24, no. 3, pp. 243–247, 1986.

[64] S. W. Huang and P. C. Li, "Ultrasonic computed tomography reconstruction of the attenuation coefficient using a linear array," *IEEE Trans. Ultrason. Ferroelectr. Freq. Control*, vol. 52, no. 11, pp. 2011–2022, 2005.

[65] Y. Fujii, N. Taniguchi, K. Itoh, K. Shigeta, Y. Wang, J. W. Tsao, K. Kumasaki, and T. Itoh, "A new method for attenuation coefficient measurement in the liver comparison with the spectral shift central frequency method," *J. Ultrasound Med.*, vol. 21, no. 7, pp. 783–788, 2002.

[66] M. Sasso, M. Beaugrand, V. De Ledinghen, C. Douvin, P. Marcellin, R. Poupon, L. Sandrin, and V. Miette, "Controlled attenuation parameter (CAP): a novel VCTE™ guided ultrasonic attenuation measurement for the evaluation of hepatic steatosis: preliminary study and validation in a cohort of patients with chronic liver disease from various causes," *Ultrasound Med. Biol.*, vol. 36, no. 11, pp. 1825–1835, 2010.